



Evolutionary analysis of Slc11 mechanism of proton-coupled metal-ion transmembrane import

Mathieu F. M. Cellier

► To cite this version:

Mathieu F. M. Cellier. Evolutionary analysis of Slc11 mechanism of proton-coupled metal-ion transmembrane import. AIMS Biophysics, 2016, 3 (2), pp.286 - 318. 10.3934/biophy.2016.2.286 . pasteur-01535408

HAL Id: pasteur-01535408

<https://riip.hal.science/pasteur-01535408>

Submitted on 8 Jun 2017

HAL is a multi-disciplinary open access archive for the deposit and dissemination of scientific research documents, whether they are published or not. The documents may come from teaching and research institutions in France or abroad, or from public or private research centers.

L'archive ouverte pluridisciplinaire **HAL**, est destinée au dépôt et à la diffusion de documents scientifiques de niveau recherche, publiés ou non, émanant des établissements d'enseignement et de recherche français ou étrangers, des laboratoires publics ou privés.



Distributed under a Creative Commons Attribution 4.0 International License



Research article

Evolutionary analysis of Slc11 mechanism of proton-coupled metal-ion transmembrane import

Mathieu F. M. Cellier

Inrs-Institut Armand-Frappier, 531, Bd des prairies, Laval, QC H7V 1B7, Canada

Correspondence: E-Mail: mathieu.cellier@iaf.inrs.ca; Tel.: +1-450-687-5010 (ext. 4681);
Fax: +1-450-686-5301.

Abstract: Determination of the crystal structure of ScaDMT, a member of the Slc11 family, provided opportunity to advance understanding of proton-dependent metal-ion uptake by interfacing Slc11 molecular evolution and structural biology. Slc11 carriers belong to the ancient and broadly distributed APC superfamily characterized by the pseudo-symmetric LeuT-fold. This fold comprises two topologically inverted repeats (protomers) that exchange alternate configurations during carrier cycling. Examining ScaDMT molecule inserted within a model membrane allowed to pinpoint residues that may interact with surrounding lipid solvent molecules. Three-dimensional mapping of Slc11-specific sites demonstrated they distribute at the protomer interface, along the transmembrane ion-conduction pathway. Functional sites were predicted by modeling hypothetical ScaDMT alternate conformers based on APC templates; these candidate homologous sites were found to co-localize with Slc11-specific sites, a distribution pattern that fits the functional diversity in the APC superfamily. Sites that diverged among eukaryotic Slc11 (Nramp) types were located in transmembrane helices that may participate in discrete steps during co-substrate translocation, suggesting these sites influence transport activity. Adding some functional dimension to Slc11 carrier evolution will inform molecular understanding of metal-ion transport selectivity and regulation, Slc11 physiological roles and contribution to host resistance to microbial infection.

Keywords: metal-ion; membrane transport; proton-coupling; solute carrier family 11; proton-dependent Mn transporter; natural resistance-associated macrophage protein; divalent metal transporter; LeuT fold; amino acid-polyamine-organo-cation superfamily.

Abbreviations:

Slc: Solute carrier;

MntH: Proton-dependent Mn transporter;
 Nramp1: Natural resistance-associated macrophage protein 1;
 Dmt1: Divalent metal transporter 1;
 APC: Amino acid-polyamine-organocation;
 TMS: Transmembrane segment.

1. Introduction

Slc carriers are solute membrane transporters that can either facilitate passive transfer of a substrate down its concentration gradient or catalyze secondary-active transport using the energy stored in the electrochemical gradient of a driving ion (e.g., Na^+ , H^+). The HUGO Gene Nomenclature Committee recognizes 52 SLC families, represented by 395 genes that constitute the largest portion of the human complement of membrane transporters (826 genes in total; [1]). About 15% of SLC families are specific for various metal-ions (e.g., Ca^{2+} , Mg^{2+} , Zn^{2+} , Fe^{2+}), including SLC11 carriers which use the proton motive force to catalyze cytoplasmic import of several transition metal-ions (Fe^{2+} , Mn^{2+} , Co^{2+} , Cd^{2+} ; [2]). The human SLC11 family comprises two genes, *SLC11A1* (*NRAMP1*) and *SLC11A2* (*DMT1*) which are conserved in tetrapods whereas *DMT1*-like genes are present as well in lower vertebrates, including ray-finned fishes [3,4].

The Slc11 family is more broadly conserved both in prokaryotic and eukaryotic organisms. Slc11 carriers primarily mediate nutritional functions by facilitating cellular provision of metal-ions that are biochemical co-factors of vital importance. Slc11 metal substrates also represent key resources most coveted during infection by both host and invading microbes [5]. Prokaryotic Slc11 (MntH) and eukaryotic Slc11 (Nramp) thus represent factors of microbial virulence and host resistance, respectively.

In amoeba as in human macrophages Nramp carriers serve both nutritional and antimicrobial purposes coupled to phagocytosis: absence of Nramp1, the isoform that is specifically expressed in the membrane of lysosomes from these professional phagocytes, results in uncontrolled replication of and natural susceptibility to infection by intracellular parasites enclosed in a phagocytic vacuole (phagosome), such as Mycobacteria, Salmonella and Leishmania spp. [6,7]. It thus seems that Nramp expression in the membrane of endosomal vacuoles has been evolutionary conserved because it ensures transition metal-ion import into the cytoplasm and contributes to host survival in the face of microbial infection.

The three-dimensional (3D) structure of a bacterial member of the Slc11 family, ScaDMT, was recently determined. It revealed an architecture common to other Slc families (e.g., Slc5, 6, 7, 12 and 38) that otherwise display low level sequence similarity [8]. These structurally related Slc families together belong to the APC superfamily, which was defined by phylogenetic analyses and topology prediction identifying a 10 TMS common core [9]. This 10 TMS hydrophobic core corresponds to a conserved fold, the LeuT fold, named after the first transporter whose structure was elucidated and which represents the Slc6 family [10].

A hallmark of the LeuT fold is its internal 3D structure: it is made of two direct repeats (protomers) comprising 5 TMS each, which thus adopt inverted topologies; protomer association creates at the interface a central permeation pathway that is required for carrier function [11]. The protomers are pseudo-symmetric because the sequences encoding them diverged widely; this may

have aided adaptation of the LeuT-fold to various substrates and transport modes, by favoring preferential conformations for example. LeuT-fold protomers also demonstrate asymmetry by co-existing in alternate configurations they swap during alternate-access transport cycle [11]. Comparison of structure-function relationships among families that constitute the APC superfamily implies a common origin and indicate the LeuT fold is evolutionary ancient [9].

The first transmembrane helix of each protomer of the LeuT fold is interrupted in its middle, by a short extended peptide that provides contact sites to bind solute substrates [11–13]. Depending on APC families, TMS1 residues may also contribute to bind the cation that drives transport while TMS6 may rather interact with the transported substrate only, indicating a degree of functional divergence between pseudo-symmetric repeats [14]. The third TMS of each repeat (TMS3 and 8) fold as long parallel helices that occupy diagonal positions, their central portions facing TMS1 and 6 extended peptides. TMS3 and 8 also contain residues that may interact with cosubstrates to occlude the binding sites from surrounding solvent once they are liganded; a process described as formation of a thin gate ([13,15]; Figure 1).

Besides, TMS1 and 6 form with TMS2 and 7 a compact four-helix bundle. During carrier cycling the "helical bundle" rocks around a central axis parallel to the membrane plane, a step that is part of the alternate gating mechanism that contributes to form thick gates (~20Å thickness, made up of packed TMSs; [13–15]; Figure 1). In contrast, TMS3, 4, 8 and 9 form a "hash motif", with TMS4 and 9 perpendicular to the membrane plane. This "hash motif" undergoes minimal movement during transport cycle. Intramolecular oscillation of the "helical bundle" relative to the "hash motif" forms the basis of the transporter alternate gating mechanism, which ensures that cosubstrate binding sites are accessible from only one side of the membrane at a time (Figure 1).

The two remaining pseudo-symmetric parts of the LeuT fold (TMS5 and 10) also undergo alternate rearrangements during transport cycling; they contribute to form thick gates that insulate the liganded cosubstrate binding sites from internal or external solvent, respectively. The segment connecting TMS9 and 10 (loop 9/10) forms with TMS10 part of the external thick gate that closes as the "helical bundle" rocks together with bound cosubstrates towards the cell interior. Loop 4/5 and TMS5 are part of the internal thick gate that opens to make way for co-substrates towards the cytoplasm.

Compiling known 3D conformations of transporters from the APC superfamily led to propose a series of states that occur during cation-driven transport cycle [14,16] (Figure 1). Though similar, carrier cycling steps vary between different transporters. Several reasons may be invoked such as the mode of transport (symport or antiport), nature of the driving cation (e.g., Na⁺ or H⁺) and its number of binding sites as well as the type of transported substrate (amino acid, sugar, nucleobase or metal). Hence, comparing similar snapshots of LeuT and Mhp1 transport cycles reveals differences in the timing and amplitude of intramolecular movements. Nevertheless the various conformations established for several APC carriers [10,14,17–31] allow homology modeling of hypothetical intramolecular rearrangements that may relate to discrete steps in Slc11 carrier cycling.

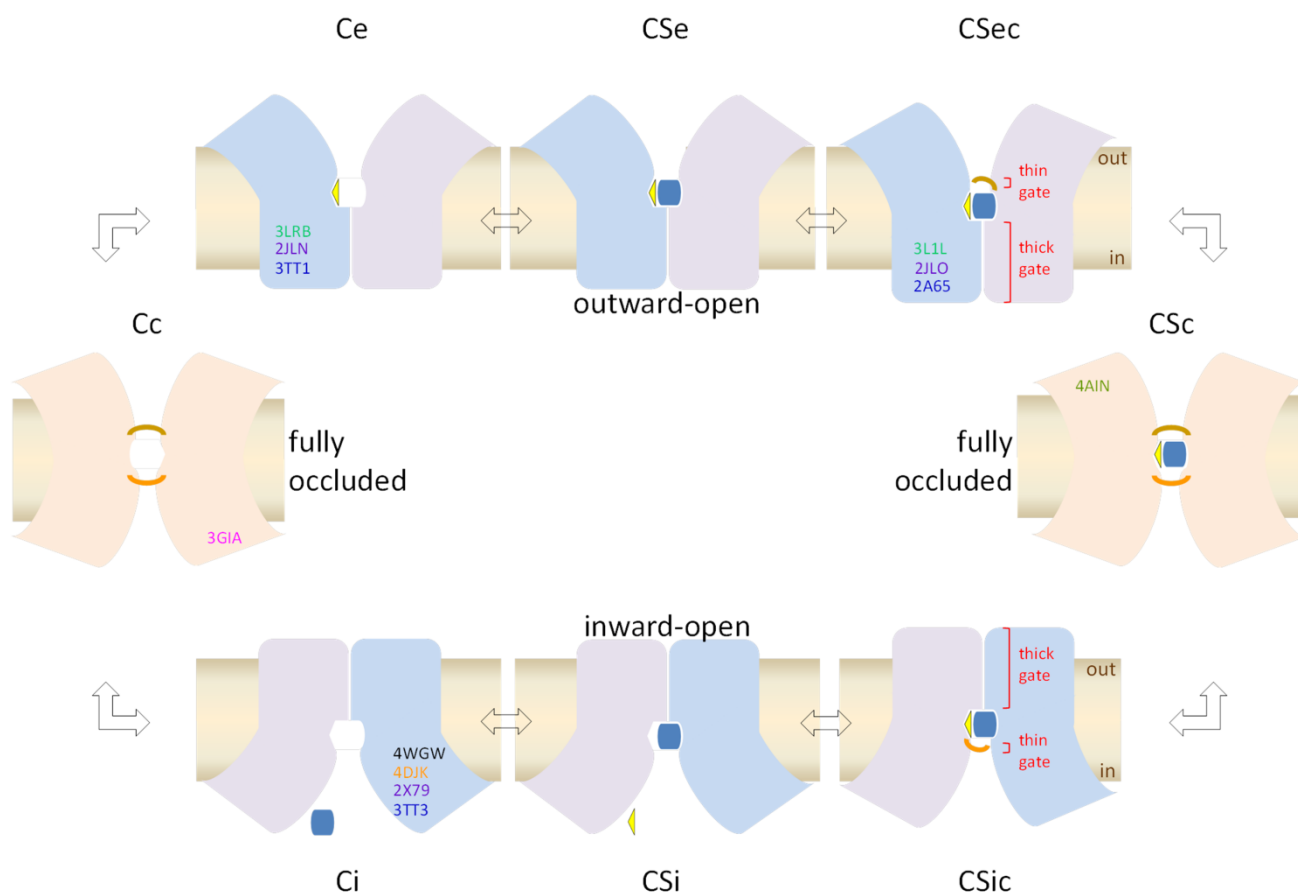


Figure 1. Hypothetical transient conformations during proton-coupled cycling of Slc11 carriers. The LeuT-fold that typifies carriers of the APC superfamily is depicted as a pair of pseudo-symmetric protomers with inverted orientations and alternate configurations (light blue, light purple). Carrier outward open conformations are shown on top: the apo form (Ce) may be stabilized by binding an external proton (yellow triangle) which favors recruitment of divalent metal substrate (dark blue box; CSe), a step followed by occlusion of the co-substrate binding sites (CSec) by a thin external gate (light brown). A dually occluded, symmetrical transient state (CSc, right) allows transition toward inward-open conformations shown at the bottom. Inward-open conformations are pseudo-symmetrically related to outward-open conformations: an occluded conformation (CSic) transitions to an open state facilitating proton release (CSi) before substrate is unloaded on the cytoplasmic side of the membrane (Ci), leaving an apo-form that becomes fully occluded (Cc, left) to rapidly switch back to outward open conformations and complete carrier cycle. Co-substrate diffusion is prevented by closing/opening of carrier gates, shown in red: alternately open conformations are closed on the opposite side of the membrane by a thick gate whereas carrier bound cosubstrates are transiently protected from open solvent access by a thin gate. The structures of carriers from the APC superfamily, which represent discrete steps of transport cycle that were studied in this work, are indicated by Protein Data Bank accession codes (dark blue, LeuT; purple, Mhp1; dark green, AdiC; light green, BetP; orange, GadC; pink, ApcT; black, ScaDMT).

The 3D structure determined for a bacterial member of the Slc11 family, *Staphylococcus capitis* DMT (ScaDMT), revealed an inwardly open conformation that allowed visualizing the binding of metal substrates [8]. In this conformation (Ci) the internal thin and thick gates are both opened to allow access to the cytoplasmic solvent from the substrate binding site. Metals previously shown to be transported by Slc11 carriers were fully coordinated by the substrate binding site, including Mn^{2+} , Fe^{2+} , Co^{2+} , Cd^{2+} , as well as Pb^{2+} and Ni^{2+} . The four residues contacting metal substrates appeared organized pseudo-symmetrically, locating in the extended peptide segments that interrupt TMS1 and 6 in their middle [8].

Despite the wealth of structural information that ScaDMT 3D structure conveys, additional data are necessary to gain detailed understanding of the mechanism of Slc11 H^+ and Me^{2+} symport. This will require elucidating the discrete intramolecular interactions and rearrangements that take place during carrier cycling. Due to difficulty in crystallizing different conformations of a same transporter it is desirable to envisage complementary strategies such as evolutionary based analyses that include homology modeling and prediction of key functional residues.

Residues forming ScaDMT inwardly open substrate binding site are evolutionary conserved and specific to Slc11 carriers [32]. Multiple sequence alignment of Slc11 family members and representatives of the group of sequences most closely related to, albeit phylogenetically distinct from, Slc11 carriers revealed few sites corresponding to residues that are strictly conserved in each group but differing between them (Slc11 family vs outgroup). Such sites may represent type II evolutionary rate-shifts possibly underlying radical functional changes [33–36].

Analyzing multiple sequence alignments representing protein families can reveal evolutionary rate variation among sites but understanding the underlying phenomena is not straightforward, in part because many molecular traits may correlate with site-specific mutation rate [37,38]. These include structural constraints (e.g., domain structure, structural disorder, flexibility, solvent accessibility, inter-chain contacts), functional constraints (e.g., catalytic activity, co-evolution at interfaces) as well as environmental constraints (expression level and timing, subcellular localization and chaperone targeting). Consequently, current models can explain about 60% of the observed variance in evolutionary rate variation among sites.

The importance of co-evolving residues for protein specific activity and/or structure-function coordination is also well established, and optimized handling of phylogenetic information has improved the capacity to predict contacts between (distal) residues [39,40]. Accordingly, phylogenetic inference using accurate model of among-site heterogeneity allows detecting specificity-determining positions by examining sequence conservation among different branches of a phylogenetic tree [37,40].

Slc11 phylogenetic outgroup was recently identified as a novel family of Mg^{2+} transporters [41] whereas functional testing of Slc11 candidate type II rate-shifted sites revealed specific roles in (co)substrate interactions [32,42]. Functional distinction of the Slc11 family from its phylogenetic outgroup thus allows to examine site by site variations in substitution rate among these groups and to identify Slc11-specific residues that may exert key functional roles. Further definition of Slc11 main phylogroups (prokaryotic MntH groups A, B C and eukaryotic prototype and archetype Nramps [43–45]) enables to investigate intra-family diversification and its potential impact on carrier activity. For instance, it is of interest to determine whether emergence of archetype and prototype Nramp, which occurred early in eukaryote evolution, resulted in functional divergence.

To identify Slc11- and Nramp type-specific sites multiple sequence alignments representing the

evolutionary bifurcations between either the Slc11 family and its outgroup or prototype and archetype Nramps were used to examine sites demonstrating phylogroup-specific variations. To evaluate whether these candidate rate-shifted sites may relate to functional roles their 3D location was mapped onto ScaDMT structure, taking into consideration residues previously predicted to interact with lipid molecules using ScaDMT structure embedded in a model membrane. To examine sites that may be homolog to catalytic residues from other APC carriers, hypothetical ScaDMT conformers were modeled using available APC templates and ScaDMT residues superimposing onto APC carrier catalytic sites were identified. The distribution of both sets of sites, candidate evolutionary rate-shifts and/or hypothetical APC homologs, were then mapped onto ScaDMT structure.

These analyses indicate spatial overlap in the distributions of Slc11 predicted type II rate-shifts and sites corresponding to residues known to bind co-substrates from 3D structures of APC carriers. The majority of Slc11-specific sites locate at the interface of LeuT-fold protomers, suggesting direct functional roles, whereas a fraction of these sites may interact with lipids (about 30%). Sites that evolved among eukaryotic Nramp map to areas of ScaDMT structure that may contribute to regulating Slc11 carrier activity, including interactions with membrane lipids. Data together support the notion that Slc11 carrier evolution fits the paradigm of LeuT-fold based structure-function relationships on the one hand (rocking bundle mechanism) while pointing at structural divergences that may reflect Slc11-specific activity, as previously observed for other families of the APC superfamily.

2. Materials and Methods

2.1. Sequence analyses

A set of 387 aligned sequences was derived from a multiple sequence alignment containing 665 entries that comprised the Slc11 family and its phylogenetic outgroup, including representatives of prokaryotic Slc11 carriers (MntH, groups A, B and C) and eukaryotic Slc11 carriers (Nramp/Dmt, prototype and archetype; [43]). Briefly, Phi-Blast strategies [46] distinguishing Slc11 phylogroups were employed to assemble a sequence set; whole sequences were used to visualize similarity clusters representing the Slc11 phylogroups by Clans analysis (Blast all against all; [47]). Neighbor-Joining (NJ) phylogenetic analyses using MEGA6 [48] were conducted separately for each Slc11 phylogroup and the resulting trees were used to select representative sequences. 665 representative sequences were aligned using ClustalX [49] and manually edited using Seaview [50]. A global NJ tree [43] was used to derive 387 sequences representing the phylogenetic diversity of each group (number of sequences): Outgroup (19), MntH B (21), MntH A and MntH AV (91), MntH H (37), MntH Cs and prototype Nramp (142, including 119 MntH Cs and 23 prototype Nramp) and archetype Nramp (77). Another set of 126 sequences covering the principal eukaryotic supergroups ([51–53]; Metazoa, Fungi, Amebozoa, Archaeplastida, Alveolata, Stramenopiles and Rhizaria) was used separately: archetype Nramp (88), prototype Nramp (27) and MntH A_H (11). Maximum likelihood analyses were performed as previously described [43,54], using PhyML 3.0 [55]. Simple trees representing Slc11 phylogroups under study were used to derive group-specific sequence logos using Phylo-mLogo [56].

2.2. Molecular studies

Protein Data Bank entries and MemprotMD models [57] were visualized using Pymol [58]. Structure superimpositions were performed using FATCAT [59] and examined with Pymol. Structural models were generated using Modeller [60] and hypothetical missing conformers were produced using the ConTemplate pipeline [61].

3. Results and Discussion

3.1. *Slc11 carriers are highly hydrophobic integral membrane proteins*

Insertion of ScaDMT 3D structure in a model lipid bilayer, which was assembled and equilibrated by coarse-grained molecular dynamics simulations using the automated pipeline MemProtMD, showed the polypeptide chain is fully embedded [57]. Viewed in the membrane plane, the Slc11 protein forms a compact helical pack (Figure 2AB) that creates at its extremities openings in the surrounding lipid bilayer. A relatively small aperture on the external side of the membrane indicates the outer thick gate is closed and prevents solvent access to the lumen of the translocation pathway. The internal side of the membrane displays a larger hole letting solvent penetrate into the interior of the ion conduction pathway. Views perpendicular to the membrane plane show a larger opening on the internal face that is apparently delimited by TMS5, 8, 6 and 1 (Figure 2CD).

Note, ScaDMT structure was obtained with a N-terminally truncated polypeptide chain that lacked the first half of TMS1 (TMS1a) yet remained functional [8]. As a result, the internal membrane leaflet modeled in place of TMS1a is significantly distorted (Figure 2B, 2D). A marked depression of the lipid surface fills the space left vacant by TMS1a absence and accentuates the access to the translocation pathway (Figure 2D), while loops connecting TMS8/9 and TMS2/3 create a slight lipid protrusion on the opposite side of the membrane opening (Figure 2D, inset).

Because the Slc11 protein is integrally solvated in the membrane, polar and/or potentially charged residues within TMSs are expected to follow selective spatial distribution determined in part by the asymmetric lipid composition of native membranes [57]. Unexpected location may instead reflect other types of chemical interaction, for example inter-helix contacts and/or binding of solvent or solute molecules. Examining Slc11 substitution profile at such sites may thus reveal conserved residues with functional roles. Slc11 TMS1, 3, 8 and 6 are remarkable in that regard, showing several conserved polar/potentially charged residues in their middle portion (Y-DPGN⁵², D--E--G¹³⁰, G--ST/S³³¹ and MPH²²⁸, respectively), in accordance with established structure-function relationships for the LeuT-fold [15,62].

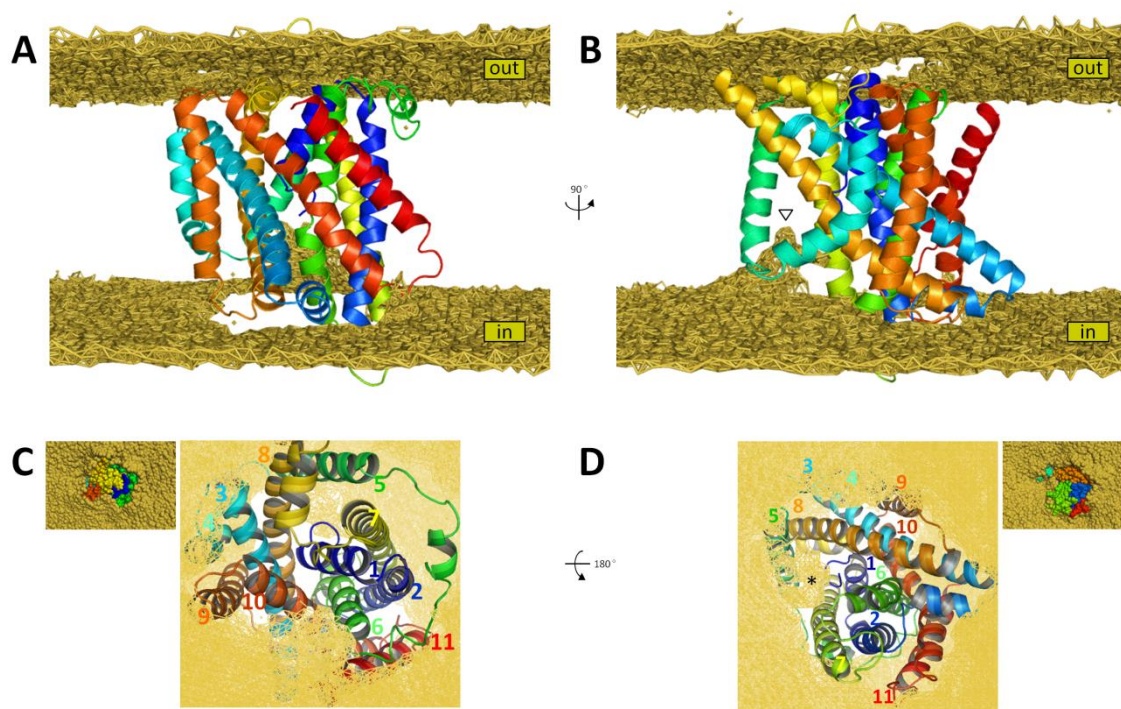


Figure 2. Representation of Molecular Dynamics simulation of ScaDMT structure (4WGW) embedding in a model membrane formed by dipalmitoylphosphatidylcholine molecules [57]. A, B. Cartoon depiction of ScaDMT structure shows the membrane interior filled with the ten TMS forming the pseudo-symmetric protomers of the LeuT-fold (TMS1-5, blue to dark green; TMS6-10, light green to red) plus TMS11 (dark red). Images in panel A and B differ by a 90° rotation around a vertical axis perpendicular to the membrane plane. C, D. Views from top (C) and bottom (D) of the model membrane and ScaDMT external and internal faces, respectively; inset: space-filled drawings showing the membrane openings created on each side of the membrane by insertion of ScaDMT inwardly-open structure. The symbols ∇ and $*$ indicate model membrane deformation due to the absence of TMS1a (B and D, respectively).

3.2. *Slc11-specific sites locate at the protomer interface along the transmembrane ion-conduction pathway*

The majority of Slc11 conserved polar, or potentially charged, residues in TMS1, 3, 6 and 8 either distinguish the family from its phylogenetic outgroup (representing type II evolutionary rate-shifts; [32]) or are invariant (i. e., conserved in the outgroup as well). Among these, TMS1 Slc11-specific segment D⁴⁹--N⁵² forms half of the metal binding site in ScaDMT inwardly open conformation, and Slc11 TMS6 M²²⁶ is part of the other half metal binding site [8]. This suggests that surveying Slc11-specific transmembrane sites may help locating amino acid residues key for carrier function.

Using a panel of 387 sequences representing Slc11 phylogroups and outgroup [43] a total of 24

Slc11-specific residues were identified (Table 1), including the four residues that constitute ScaDMT metal binding site [8]. Transmembrane helices that display several Slc11-specific sites include TMS1 and 3 (five each) and TMS6 and 8 (3 each), which indicates that more than half of Slc11-specific sites are located at the protomer interface.

Ten Slc11-specific sites may represent homologs (or structural neighbors) of residues previously shown to interact with co-substrates in a sample of structures from various carriers of the APC superfamily (MhsT, BetP, AdiC and CaiT; [14,24,30,31]). These candidate homologous sites, found predominantly in TMS1, 3 and 6 (3 each), TMS7 (2) and 8, 9, and 10 (one each), were suggested by conformer homology modeling using the ConTemplate approach [61]. For this, relaxed parameters were used to take into account the low level of sequence identity and moderate level of structural similarity within the APC superfamily (Rmsd: 3.75 Å, Q-score: 0.15, % coverage: 45; Narunsky & Ben-Tal, person. comm.).

Of 14 Slc11-specific residues either known or presumed to exert functional roles (Table 1), only three seemed to interact with modeled lipids [57]: TMS1 Y⁴⁷ (lipid head; might be an artifact due to TMS1a truncation), TMS3 A¹¹⁹ and TMS10 L³⁹² (lipid tail, minor interactions). These data imply corroborating 3D locations, between Slc11-specific rate variants and candidate homologous sites of APC carriers from various families (e.g., Slc6, Slc12), supporting the notion that Slc11 sites which represent type II evolutionary rate-shifts may exert functional roles.

Table 1. ScaDMT residues corresponding to Slc11-specific sites (+) or candidate functional sites predicted by homology threading using APC carriers from various families.

Slc11-sp (stick)	Slc11 (vs outG) [‡]	color code [‡]	functional role [§] (hypoth.)	APC family [#]	deleterious mutation (expermt.)	lipid interact.
ScaDMT residues*						
TMS1						
V ⁴⁵	+	V,I (A)	split pea			-
Y ⁴⁷	+	Y,F (F)	blue sky	S, Na1	M, A	head
M ⁴⁸	-	n.a.	light purple	Na2	M	head
D ⁴⁹	+	D (G)	red	Metal	D	+
P ⁵⁰	-	P	light pink	S	A	-
G ⁵¹	-	G	dark pink	S	M, B, A	+
N ⁵²	+	N (T)	dark red	Metal, Na1	D, M	+
S ⁵⁶	+	D,N,S (C,A)	yellow			+
TMS2						
I ⁷¹	-	n.a.	light pink	S	C	-
TMS3						
A ¹¹⁶	-	n.a.	light blue	Na'	B	-
E ¹¹⁷	+	E,v (V,G,T)	yellow			+

A ¹¹⁹	+	A,v,I (G)	light pink	S	A		(tail)
I ¹²⁰	-	n.a.	raspberry	S, Na'	B, A		-
T ¹²³	+	T,c,S (Y,F)	light blue	Na'	B		-
D ¹²⁴	-	n.a.	light pink	S	A		-
A ¹²⁶	+	A,Q (G)	split pea				-
E ¹²⁷	+	E (N,D)	light pink	S	M		-
G ¹³⁰	-	n.a.	yellow			+	-
TMS4							
T ¹⁵⁰	+	T,G,A (I,M)	split pea				(tail)
D ¹⁵³	-	n.a.	yellow			+	(tail)
TMS5							
E ¹⁶⁹	-	n.a.	light purple	Na2	B		head
TMS6							
G ²²²	-	n.a.	hot pink	S	A	+	-
A ²²³	+	A (T)	magenta	Metal, S	D, M, C	+	-
T ²²⁴	-	n.a.	violet purple	S, Na1	M, B, C		-
I ²²⁵	-	n.a.	hot pink	S	B, A		-
M ²²⁶	+	M (V)	magenta	Metal, S	D, M	+	-
P ²²⁷	-	n.a.	hot pink	S	C		-
H ²²⁸	+	H (Y)	deep purple	S, Na'	B	+	-
N ²²⁹	-	n.a.	hot pink	S	C		-
L ²³²	-	n.a.	tv blue	Na'	B		-
TMS7							
D ²⁶⁰	-	n.a.	orange			+	head
A ²⁶⁸	+	A,S,G (G)	dirty violet	Na1	M		-
N ²⁷²	+	N (S,T)	olive	Na1	M	+	-
TMS8							
S ³²⁶	-	n.a.	violet	Na2	M		(head)
N ³²⁹	-	n.a.	violet	Na2	M, B		(head)
S ³³⁰	-	n.a.	violet	Na2	M		-
I ³³²	-	n.a.	violet	Na2	B		-
T ³³³	-	n.a.	warm pink	S, Na2, Na'	M, B		(head)
G ³³⁴	+	G,A (A,S)	hot pink	S	A		-
T ³³⁵	+	T,A,G (P,A)	limon				-
A ³³⁷	-	n.a.	tv blue	Na'	B		-
Q ³³⁹	+	Q,A (A)	limon				-
TMS9							
T ³⁵⁹	+	T (I,V)	tv blue	Na'	B		-

R ³⁶⁰	-	n.a.	orange		+	-
P ³⁶⁶	+	P (L,I,V)	limon			tail
TMS10						
S ³⁸⁸	+	S,L (A)	limon			(tail)
L ³⁹²	+	L,Q (N)	hot pink	S	A	(tail)
TMS11						
N ⁴³⁷	+	N,D (G,S)	limon			head

[‡]Rate variation in MntH B (MntH from anaerobic bacteria; [43]: Y⁴⁷, E¹¹⁷, T¹⁵⁰, A²⁶⁸, G³³⁴, T³³⁵, Q³³⁹, P³⁶⁶).

[¥]Residue Ca and/or side chain color (Figure 3) depending on site rate variation, predicted functional role, mutation data and protomer (N or C).

[§] Homology prediction: S: substrate binding; Na1, Na2, Na': cosubstrate (driving-cation) binding.

[#] APC families: M, MhsT; B, BetP; C, CaiT; A, AdiC and D, ScaDMT.

^{*}Residues mutated and conserved among Slc11-derived plant transporters of Al³⁺ ([63,54]: G⁵¹, T¹²³, M²²⁶, H²²⁸, S³³⁰, T³³³, G³³⁴).

Regarding the remaining Slc11-specific residues (10 in total), four were suggested to interact with lipids, two mildly with lipid tails (TMS4 T¹⁵⁰ and TMS10 S³⁸⁸) and two with either lipid head (TMS11 N⁴³⁷) or tail (TMS9 P³⁶⁶). Overall, 70% of Slc11-specific residues were not expected to interact with lipids as ScaDMT structure was membrane embedded [57], and a majority of them (14/24) were either predicted or shown to interact directly with Slc11 cosubstrates. These data indicate a phylogenetic approach is useful to detail Slc11 carrier structure/function relationships and to identify target sites for mutagenesis studies.

3.3. Candidate APC homologous sites co-localize with Slc11-specific residues

Implementing the ConTemplate approach with relaxed parameters yielded 19 additional sites that represent candidate homologs (or structural neighbors) of residues previously shown to interact with various cosubstrates in APC carriers (MhsT, BetP, AdiC and CaiT; [14,24,30]; Figure 3 and Table 1).

These 19 potential functional sites map to TMS6 (six), TMS8 (five), TMS1&3 (three each) and TMS2&5 (one each); they generally appear proximal to Slc11-specific sites. TMS6 and 8 enrichment in candidate homologous sites contrasts with TMS1 and 3 high proportion of Slc11-specific residues (Table 1), further substantiating Slc11 protomer asymmetry previously noted with variations in sequence conservation, polypeptide length and hydropathy profile [62].

Although not Slc11-specific the predicted APC homologous sites are in majority conserved among the 387 sequences studied, with eight invariant or almost invariant sites, four highly conserved (two possible residues), five moderately variable (up to four substitutions per site) and two variable sites. LeuT-based structural homology approach thus points at conserved Slc11 sites, supporting potential functional roles for the corresponding residues.

Of these 19 putative APC homologous sites, a fraction (five) corresponded to ScaDMT residues apparently interacting with modeled lipids [57]: TMS1 M⁴⁸ (lipid head, possible artifact due to TMS1a absence, as suggested by AtNramp4 L⁶⁷ role in Cd²⁺ selectivity; [64]), TMS5 E¹⁶⁹ (lipid head)

and TMS8 S³²⁶, N³²⁹ and T³³³ (lipid heads, minor interactions). The majority of these sites (14/19) cluster at positions neighboring Slc11-specific residues, notably as part of TMS1, TMS3, TMS6 and TMS8 (Table 1, Figure 3) which form the LeuT fold functional interface [11,37]. Accordingly, these candidate APC homologous sites may contribute structural and/or functional interactions important for Slc11 activity.

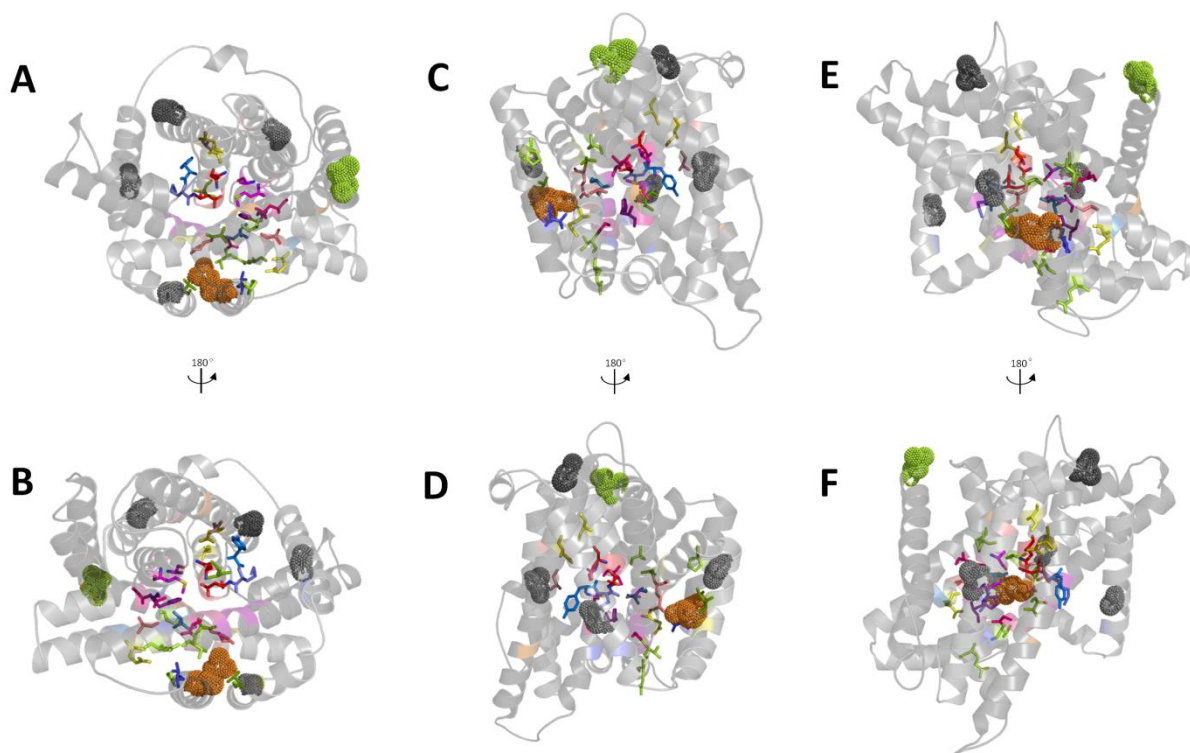


Figure 3. Location of Slc11-specific residues on ScaDMT inwardly open structure (4WGW; [8]). Views A, C, E and B, D, F are respectively rotated by 180° around a central axis either parallel (A, B) or perpendicular (C,D and E,F) to the membrane plane. Panels A and B represent views from top and bottom of the membrane, respectively, and panels C-F, transversal views. Panels C, E and D, F illustrate views rotated by 90° around a vertical central axis. Slc11-specific residues are represented by sticks. Functional sites predicted by homology threading of hypothetical conformers [61] are indicated by coloring the molecule Cα trace, depending on their putative role and protomer (amino or carboxy), as well as sites whose mutation impairs Slc11 activity (cf Table 1). DMT1 (SLC11A2) mutations with deleterious effects are shown as dotted spheres.

In particular, a pair of sites in ScaDMT TMS8 may be homologous to LeuT adjacent residues that are part of Na²⁺ binding site and which were shown to stabilize LeuT outwardly-open conformation [27,65]. The corresponding pair of Slc11 residues is highly conserved (Table 1; N³²⁹ and S³³⁰; Consurf classes, respectively 8 and 9 of 9 [66]) and may thus participate in proton-dependent metal transport.

Overall, the selective distribution of Slc11-specific residues and candidate APC homologous sites at the protomer interface differs, for instance, from the location of residues/sites that were found

mutated in DMT1 protein of patients affected with microcytic anemia and iron accumulation in the liver [67–73]. *DMT1* disease-causing mutations rather affect sites that are part of the external fence of the molecule (Figure 3); three of them correspond to variable sites while four are conserved either in eukaryotic Nramp only or both in Slc11 family and outgroup.

3.4. Family-specific functional adaptation of the LeuT-fold

To illustrate both the central importance and family-specificities of the protomer interface formed by TMS1, 3, 6 and 8, which connect the LeuT-like helical bundle and hash motif, the relative positions of these helices was compared between LeuT and Mhp1 structures in three distinct conformations: outward-open (Ce; [18,27]), outward-open occluded (after substrate binding; CSec; [10,74]) and inward-open (Ci; [25,27]). The relative motion of the carrier outer fence (TMS2, 4, 5, 7, 9 and 10) is demonstrated separately for clear visualization (Figure 4).

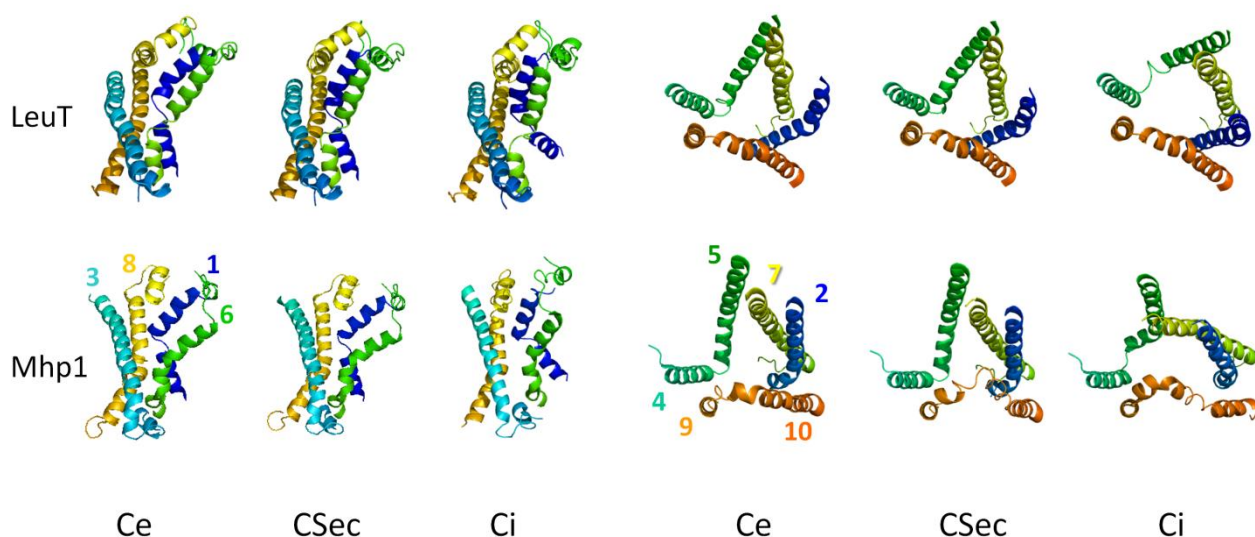


Figure 4. Illustration of intramolecular rearrangements during APC carrier cycling. LeuT (Slc6, top panel) and Mhp1 (bottom panel) structures represent distinct families of the APC superfamily. Three steps in APC carrier cycling are presented: outwardly-open (Ce, 3TT1 and 2JLN), outwardly-open and occluded after cosubstrate binding (CSeq, 2A65 and 2JLO), and inwardly-open (Ci, 3TT3 and 2X79) allowing cosubstrates release intracellularly (cf Figure 1). In each case the transporter structure is represented in two separate pseudo-symmetric ensembles: the protomer interface (TMS1, 3, 6 and 8), which forms an interior cavity that leads to the cosubstrate binding sites that allow translocation toward the cell interior, and the carrier outer fence, which includes gate components (TMS2, 4, 5, 7, 9 and 10).

Comparison between the two carriers shows a common mode of transport: once loaded with cosubstrates the helical bundle (TMS1, 2, 6 and 7) rocks towards the hash motif, with TMS3 and 8 standing in front relatively fixed, while parts of TMS9 and 4 undergo pseudo-symmetric rearrangements, together with TMS10 and 5, respectively, to close the outer gate and open the

intracellular gate.

LeuT and Mhp1 structures also exhibit clear differences, both in timing and amplitude of the helical bundle rocking. They differ as well in the manner the internal and external gates are operated, either for opening (TMS4, 5, 7) or for closing (TMS2, 9, 10; Figure 4). Hence, the similar mode of cosubstrate translocation imposed by a common 3D architecture nevertheless obeys distinct rules that are family-specific, presumably resulting from separate evolution and adaptation to different substrates and/or driving cations [11].

In fact, low level sequence conservation within APC families (except Slc11), broad phylogenetic distribution of these families, and the basic nature of the substrates transported (nucleobases, metals, amino acids, sugars) together suggest the APC superfamily is very ancient, which may explain in part the extent of functional divergence among APC families. In this regard it will be interesting to examine whether LeuT-like transmembrane helices that interact with cosubstrates (e.g., TMS1, 3, 6 and 8) might have been part of the vocabulary of ancient peptides [75].

The corollary of APC diversity is that family-specific details in the mechanism of solute transport can hardly be extrapolated from one family to another [65]. Yet, divergence between families may have operated in common 3D areas of the ancestral LeuT fold, so that specific determinants from one family may help locate functional features in another family. This proposition was tested using homology models that represent hypothetical ScaDMT missing conformations, which were inferred using the ConTemplate approach [61]. For clarity, the protomer interface (TMS1, 3, 6 and 8) and carrier outer fence (TMS2, 4, 5, 7, 9 and 10) were visualized separately (Figures 5 and 6, respectively).

Regarding the external fence (Figure 6), ScaDMT native inward open structure is obviously much alike the homologous models representing similar conformation (Ci: based on GadC, [28] and Mhp1, [25]), with loops connecting TMS4/5 and 9/10 demonstrating, respectively an open/relaxed internal gate and a closed/constrained external gate (despite unrefined loop modeling). ScaDMT model based on ApcT apo- inward conformation (Cc; [21]) also appears similar (yet with loop 9/10 truncated). Modeling an intermediate conformation with both cosubstrates loaded suggested both gates may be closed/constrained (CSc: BetP, [30]), whereas outward-open models (CSec and Ce: AdiC, [23] and Ce: Mhp1, [25]) display instead the loops 4/5 and 9/10 either in closed/constrained or in open/relaxed state, respectively (Figure 6).

Altogether these models indicate that ScaDMT molecule is compatible with the rocking bundle mechanism that typifies the APC superfamily. Also, use of carriers from different APC families to model comparable ScaDMT conformers, such as Ce or Ci, shows relatively similar spatial arrangement of the helices that constitute the carrier external fence (TMS2, 4, 5, 7, 9, 10). This finding corroborates observations made by comparing similar conformers of LeuT and Mhp1 carriers (Figure 4).

Modeling the interface of the helical bundle-hash motif shows a different picture (Figure 5), again reminiscent of the comparison of LeuT and Mhp1 conformers (Figure 4). Regarding inward open conformations (Ci, Cic), use of templates from three different families results in variations in the relative configuration/position of threaded helices 1, 3, 6 and 8. The appearance of the functional interface also differs between models of outward-open conformers without substrate (Ce) that were obtained using templates from two different APC families. Thus, compared to the external fence (Figure 6), modeling LeuT-like carrier functional interface shows relative structural divergence,

depending on APC templates, suggesting it reflects at least in part the variety of cosubstrates transported by APC families.

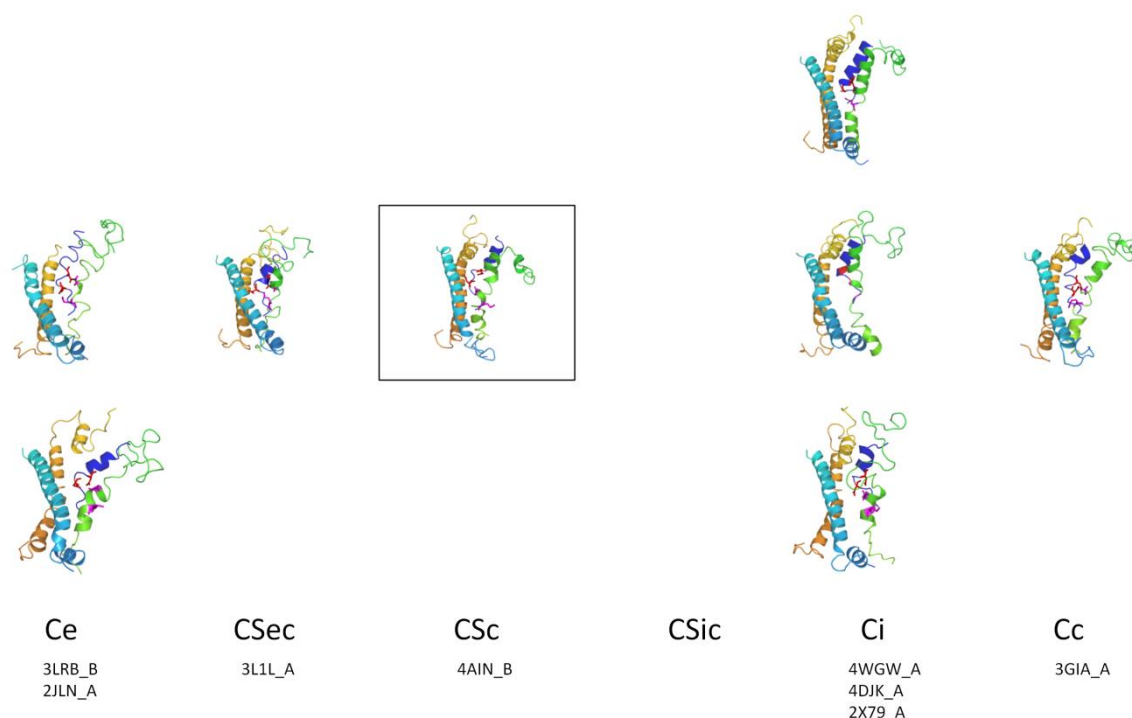


Figure 5. Predicted conformers of ScaDMT protomer interface (TMS1, 3, 6 and 8) during carrier motion for metal import (left to right). Structural models were obtained using the Contemplate approach and relaxed parameters (Rmsd: 3.75Å, Q-score: 0.15, % coverage: 45; [61]). Ce, outwardly-open; CSec, outwardly-open and occluded; CSc, fully closed and symmetric intermediate; Ci, inwardly-open; Cc, inwardly-open, occluded apo-form (cf Figure1).

This notion seems in line with the general observation that it is substrate specificity which is more likely to change within enzyme superfamilies, as diversity may result from applying a common architecture to various (co)substrates [76]. Because 75% of Slc11-specific sites cluster along TMS1, TMS3, TMS6 and TMS8 (Table 1) these helices likely determine key interactions with Slc11 cosubstrates, in agreement with the paradigm of LeuT-like carriers.

3.5. Evolutionary rate-shift analysis to elucidate Slc11 structure-function relationships

ScaDMT structure provided an essential snapshot demonstrating that Slc11 carriers belong to the APC superfamily. Understanding Slc11 mechanism of membrane transport nonetheless will require discovering the series of discrete steps that take place during carrier cycling. Solving 3D structures of distinct conformers for a single transporter is a very difficult task. This warrants pursuing predictive approaches as well, including repeat-swap modeling [77] and hypothetical conformer modeling [61].

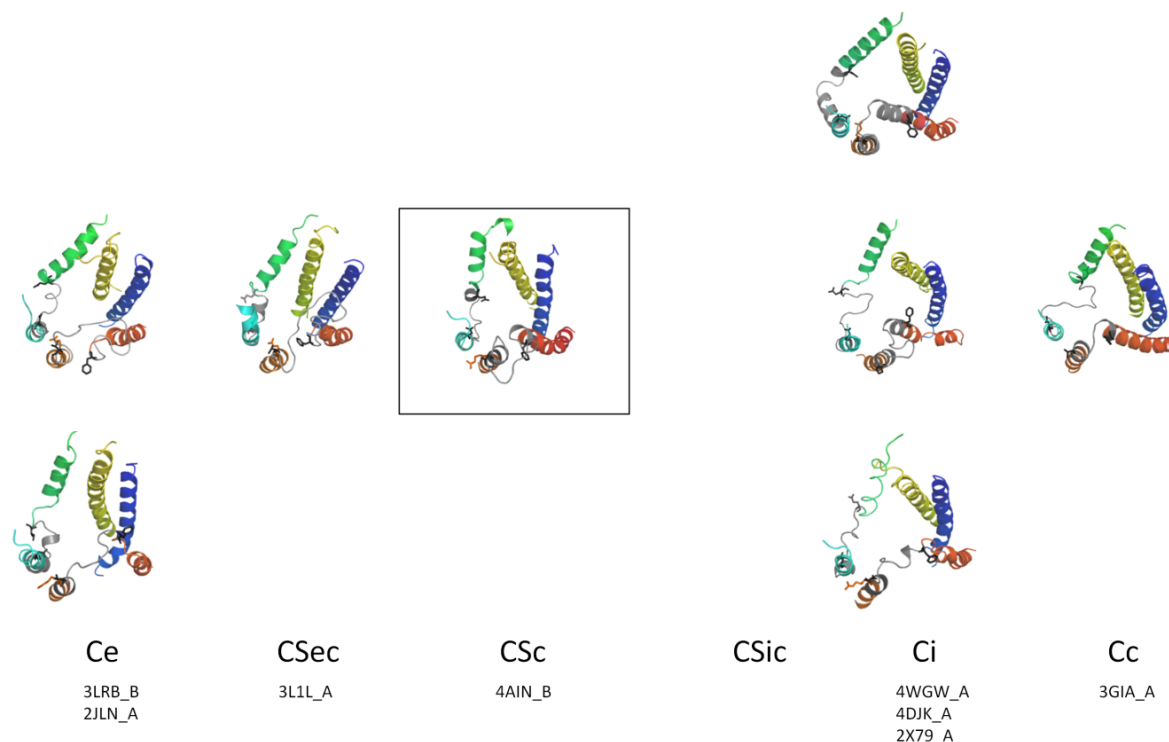


Figure 6. Model conformers of ScaDMT outer fence (TMS2, 4, 5, 7, 9 and 10) during carrier motion for metal import (left to right) obtained using the Contemplate approach. Ce, outwardly-open; CSec, outwardly-open and occluded; CSc, fully closed, symmetric intermediate; Ci, inwardly-open; Cc, inwardly-open, occluded apo-form (cf Figure 1). Loops joining TMS4/5 and TMS9/10 that are part respectively, of the internal and external gates are indicated in grey.

However, Slc11 conformer prediction is also complicated by sequence divergence both between APC families (e.g., Figure 5) and within a single family. For instance, Slc11 intervening loops are longer in the C-protomer [62] and differences in size and sequence conservation between loops involved in gating activity (i.e., TMS 4/5 and 9/10) imply dissimilar motions of the internal and external gates, respectively, during carrier cycle. Also, variations in size, tertiary structure and patterns of sequence conservation among Slc11 pseudo-symmetric TMS indicate they are subjected to different constraints (Suppl. Figure 1AB).

ScaDMT protomers display high level of asymmetry compared to other members of the APC superfamily [43], indicated by differences in the arrangement of TMS4 and 5 vs TMS9 and 10 and in the position of TMS2 and 7 (Suppl. Fig. 1ABC). Accordingly, simple swapping of protomer configurations shows obvious differences in helical organization and packing between the native template and threaded model (Suppl. Figure 1DE).

Nevertheless, native and model protomer structures superimpose without adding twists (Suppl. Figure 1). This finding suggests that ScaDMT protomers may swap alternate configurations during carrier cycling, in accordance with conformer modeling results. Yet introducing distance restraints between C taken from ScaDMT native structure, together with *ab initio* modeling, will likely be required to develop a repeat-swap modeling approach and generate pseudo-symmetric

conformers [77].

Inter-family structural divergence also may limit informativeness of homology threading of missing conformers using the ConTemplate approach [61]. Molecular adaptation to various substrates and motive forces led to family-specific variations in the architecture of the carrier translocation pathway (Figure 5), which introduce intrinsic restraints for inter-family threading approach. Length and sequence polymorphisms of TMS connecting loops also constraint the models that can be produced, at least in first approximation.

Taking advantage of family-specific sequence divergence may thus provide a complementary approach, through mutagenesis and functional analyses of sites displaying sequence variations between phylogroups. For instance, targeting Slc11-specific sites allowed identifying residues part of the co-substrate binding sites [32,42]. It is anticipated that further study of residues distinguishing the Slc11 family from its closest relative (phylogenetic outgroup: Mg^{2+} transporters; Table 1, Figure 3) will reveal mechanistic aspects of Slc11 carrier cycling. Besides, it is hypothesized that analyzing intra-family molecular evolution will reveal additional elements of Slc11 transport regulation. In turn, evolutionary-based functional studies hold potential to reveal sites whose mutagenesis may favor some conformers which could facilitate future structural studies.

Molecular evolution of the Slc11 family combines ancient origins of a conserved 3D fold with sequence properties that blend strong conservation of family-specific features with substantial diversity among Slc11 phylogroups. Accordingly, useful structural/functional information may be gained from site-directed analyses targeting evolutionary rate-shifts that distinguish either the family as a whole or some phylogroups. In particular, divergence between Nramp types may hold potentially useful information because *Nramp* gene duplication occurred early in eukaryotic evolution.

3.6. Emergence of archetype Nramp for antimicrobial defense?

Host defense genes are notoriously known to be target of evolutionary selection, essentially pathogen-driven: the Red Queen's hypothesis stipulates that hosts need evolving continually to survive pathogen encounters [78]. Accordingly, evolution from MntH to Nramp and subsequent divergence of archetype Nramp may reflect emergence of novel properties that conferred eukaryotic/host carriers a selective advantage to survive intracellular infection by restricting access to vital metal-ions.

Microbial pathogenicity relies on subverting host defenses to acquire nutrients and establish a replicative niche [78], which both depend on adequate supply of iron (and/or other metals such as manganese). To resist infection hosts must overcome the microbial armamentarium devoted to Fe and Mn capture and uptake: innate response to infection involves secreting several high affinity binding proteins that directly compete with microbial virulence factors for iron (and manganese) scavenging [79–81]. Yet successful pathogens may counter-act these defenses and hosts rely on elaborate adaptive immune responses to neutralize and/or destroy invaders.

Intracellular parasitism provides pathogens with both shelter and access to nutrient stores, such as iron labile pool and ferritin stores. Various microbial pathogens elect tissue macrophages as a replicative niche, in spite of their extraordinary antimicrobial potential, perhaps because most of body iron transit via these cells [12,43]. At homeostasis, tissue macrophages continuously recycle iron from cells eliminated through phagocytosis back into the circulation; upon infection, detection

of microbial patterns (e.g., bacterial lipopolysaccharide) induces phenotypic changes that prevent iron exit from macrophages [82,83]. By subverting macrophage innate defenses intracellular pathogens such as bacteria (*Mycobacteria*, *Salmonella*) and protozoan parasites (*Leishmania*) may thus gain access to iron sources to support their survival and replication.

Based on homologous Slc11 activities reported in amoeba and mammalian macrophages it appears plausible that proton-dependent metal import was adapted to neutralize microbial invaders early in eukaryotic cell evolution, and that it has since been conserved as a component of host nutritional immunity [12,43,78]. Though Slc11 defensive function was likely aided by co-evolution with complementary activities, such as the vacuolar proton-ATPase, it is hypothesized that eukaryotic Slc11 (Nramp) possess intrinsic properties providing some functional advantage to thwart infectious microbes.

Transition from bacterial (MntH) to eukaryotic Slc11 (Nramp) was coupled to *Nramp* gene duplication early in eukaryotic evolution since Nramp parologs were found in widely diverse taxa, including amoebae (e.g., Mycetozoa: *Dictyostelium discoideum*), plantae (e.g., red algae/Rhodophyta, moss/Bryophyta and Charophyta green algae), Glaucocystophyceae and Cryptophyta, as well as in fungi (e.g. Mucoromycotina, Glomeromycota; [5] and examples listed in Table 2). Prototype *Nramp* are absent from known animal genomes (e.g., Table 2) but some were apparently acquired horizontally by various bacterial taxa [44,45], including *S. capitis* ScaDMT. Archetype Nramp mediate host resistance to mycobacterial infection both in amoeba and human macrophages [84,85].

Table 2. Pairwise maximal BLAST scores distinguish archetype from prototype Nramp (eukaryotic Slc11 carriers; whole length sequences).

Query	archetype Nramp		prototype Nramp	
	HsaMETNR1	DdiAMB_aNR	SceASCpNR1	DdiAMB_pNR
Organism/target				
sequence type				
archetype Nramp				
Metazoa				
HsaMETaNR1	1117	455	195	258
HsaMETaNR2	653	439	175	250
DmeMET_aNR	590	483	227	295
Fungi				
BciMUCaNR4	359	419	183	277
Amoebozoa				
DdiAMB_aNR	444	997	228	314
Viridiplantae				
PpaBRYaNR1	440	479	212	306
Rhodophyta				
CmeBAN_aNR	271	268	228	280

prototype Nramp

Fungi

BciMUCpNR1	251	288	371	365
SceASCpNR1	202	243	1183	249

Amoebozoa

DdiAMB_pNR	241	295	231	1021
------------	-----	-----	-----	------

Viridiplantae

PpaBRY_pNR	229	241	219	318
------------	-----	-----	-----	-----

Rhodophyta

CmeBAN_aNR	233	249	250	369
------------	-----	-----	-----	-----

Hsa, *Homo sapiens*; Dme, *Drosophila melanogaster*; Bci, *Backusella circina*; Sce, *Saccharomyces cerevisiae*; Ddi, *Dictyostelium discoideum*; Ppa, *Physcomitrella patens*; Cme, *Cyanidioschyzon merolae*.

Based on the Red Queen's hypothesis [78] it is hypothesized that professional phagocytes (e.g., amoeba, animal macrophages) and rhizobia-infected plant cells maintained archetype Nramp expression in the membrane of endosomal vacuoles to ensure efficient iron transport into the cytoplasm, which contributed to host survival in the face of microbial infection. Accordingly, fungal archetype Nramp may play similar roles in species harboring endosymbiotic bacteria, such as *Gigaspora margarita* (Glomeromycota spp. hosting intravacuolar gram negative bacteria; [86]) and *Mortierella elongata* (Mucoromycotina spp. associated with intrahyphal gram negative bacteria; [87]).

Assuming that *Nramp* gene duplication allowed functional divergence of archetype Nramp that led to efficient antimicrobial activity of eukaryotic cells, it is suggested that examining site by site variation in substitution rate between archetype and prototype Nramp may indicate sites that have co-evolved to improve archetype Nramp function and support eukaryotic antimicrobial activity.

3.7. Evolutionary hypothesis for archetype Nramp mechanism of transport

To seek sites that co-evolved in archetype Nramp a set of 115 Nramp sequences (27 prototype and 88 archetype) was retrieved from existing databases (GenBank Nr database, Broad Institute data repository, DOE/JGI genome portal), and among site evolutionary rate variations between Nramp types were evaluated using Phylo-mLogo ([56]; Table 3). To address whether sequence divergence between archetype and prototype Nramp may point at functional determinants, variant sites were mapped onto ScaDMT structure using Pymol [58].

Table 3. Candidate evolutionary rate-shifts distinguishing archetype from prototype Nramp (eukaryotic Slc11 carriers).

	Divergent Slc11 type [‡]	Evolution. rate-shift [¥]	aNR vs (pNR)	Outgroup diverge [§]	Candidate function [#]	Lipid interact. ^{&}	Candid. residue interact. [¤]
ScaDMT residues*							
TMS1							
V ⁴⁵	a/p	(II)	I,L (V,I)	O			
G ⁴⁶		II	A (G,A)				A ²⁶⁸
M ⁴⁸	a	(II)	L,I (M,L)	(O, B)	Na2	?	
W ⁵³	a	II	L,I (W)	(O)			F ³¹⁹ , A ³²² , V ¹⁷⁹ , L ²⁷⁵
I ⁵⁴	a	(II)	E,Q (A,S)	(O)			
T ⁵⁵	a (B)	I	S,G,A (T)				
Q ⁵⁸		I	Q,N (E,A,Q,S)				
TMS2							
F ⁶⁹	p	II/I	W,F (F,W)			tail	
S ⁷⁴	a (A)	II/I	A,S,G (S,A)			(tail)	
S ⁷⁵	a (B)	(II)	T,H (N,S)	(O)			A ²⁶⁸
A ⁷⁸	a	(II)	G,A (A)	(O)			T ²²⁴ , I ²²⁵
M ⁷⁹	a	I	L,F,I (M,V,I,L)			tail	
TMS3							
A ¹²²	a	(II)	G,A (A,S)			(tail)	
T ¹²³	a	II/I	S,A,T (T,C)	O	Na ^c		<u>M</u> ²²⁶ , L ³⁹²
I ¹²⁵	a/p	I	I,M,L,V (L,I)	(O)		(tail)	
A ¹²⁶	a	(II)	Q,P (A,I)	O			<u>D</u> ⁴⁹
TMS4							
I ¹⁴⁴	a	I	W,Y (W,P,I,L)	(O)		tail	
V ¹⁵⁴		(II)	T,A (V,T)	(O)			
L ¹⁵⁷	a	II/I	F,L (I,L,F)			(tail)	
TMS5							
V ¹⁷²	a/p	(II/I)	F,I,L,V (V,I)	(O)		tail	
V ¹⁷⁹	a	(II/I)	M,L,I (I,V)	O		(tail)	W ⁵³ , A ³²²
TMS6							
T ²²⁴	a (B)	II	V,I (T)		S, Na1		A ⁷⁸
I ²²⁵	a (A)	(II)	I,V (V)		S		A ⁷⁸ , L ⁴⁰⁰
TMS7							
D ²⁶⁰	a	II	E (D,L)				

A ²⁶⁸	a	(II)	S,A (A)	(O, B)		G ⁴⁶ , S ⁷⁵
L ²⁷⁵	a/p	(II)	V,I (I)			W ⁵³
L ²⁷⁶	a	I	V,I,M,L (L)			
G ²⁷⁹		(II)	F,A (A,S)			
TMS8						
F ³¹⁹	a	(II)	W,F (F)			W ⁵³
A ³²²	a (A)	(II)	G,A (A,G)	O		W ⁵³ , V ¹⁷⁹
I ³³²		(I)	M,I,F (I,L,V)		Na2	
L ³³⁶	a	(II/I)	Y,L (L,M,I)			
I ³⁴⁰	a	(I)	F,Y,S,I (I,V,Y,F)	(O)		
TMS9						
R ³⁵⁶	a (B)	I	V,A,N (R)	(O)		
TMS10						
S ³⁸⁸	a	I	L,I,S,V,A (S)	O	(tail)	
Q ³⁸⁹	a	II	N,S (Q)			<u>D⁴⁹</u> , <u>A²²³</u>
L ³⁹²	a	(II)	Q,L (L)	O	S (tail)	<u>T¹²³</u> , <u>M²²⁶</u>
L ⁴⁰⁰	a/p	(II/I)	L,I,V (V,I,L)	(O)		I ²²⁵

Underlined: residues part of ScaDMT metal-ion binding site.

[≠] a, archetype nramp; p, prototype Nramp; A, MntH A; B, MntH B.

[¥] Candidate evolutionary rate shifts: I, type I; II, type II; I/II, intermediate.

[§] Site showing also divergence of Slc11 outgroup (O) and of MntHB group (B).

[#] Homology prediction: S: substrate binding; Na1, Na2, Na': cosubstrate (driving-cation) binding.

[&] Coarse-grained molecular dynamics simulations [57].

[‡] Residues within interacting distance (<5 Å).

*Residues also mutated, and conserved among Slc11-derived plant transporters of Al³⁺ ([54;63]: S⁷⁵, A¹⁷², T¹²³).

Overall 38 sites were identified (Figure 7), which distribute across the TMS constituting the LeuT fold. They exhibit relatively type-specific rate variations between prototype and archetype Nramp (candidate type I and/or type II evolutionary rate-shifts, Table 3). Type I rate-shift represents a scenario when, comparing two groups, sequence variation is observed in one group while conservation prevails in the other [33–36].

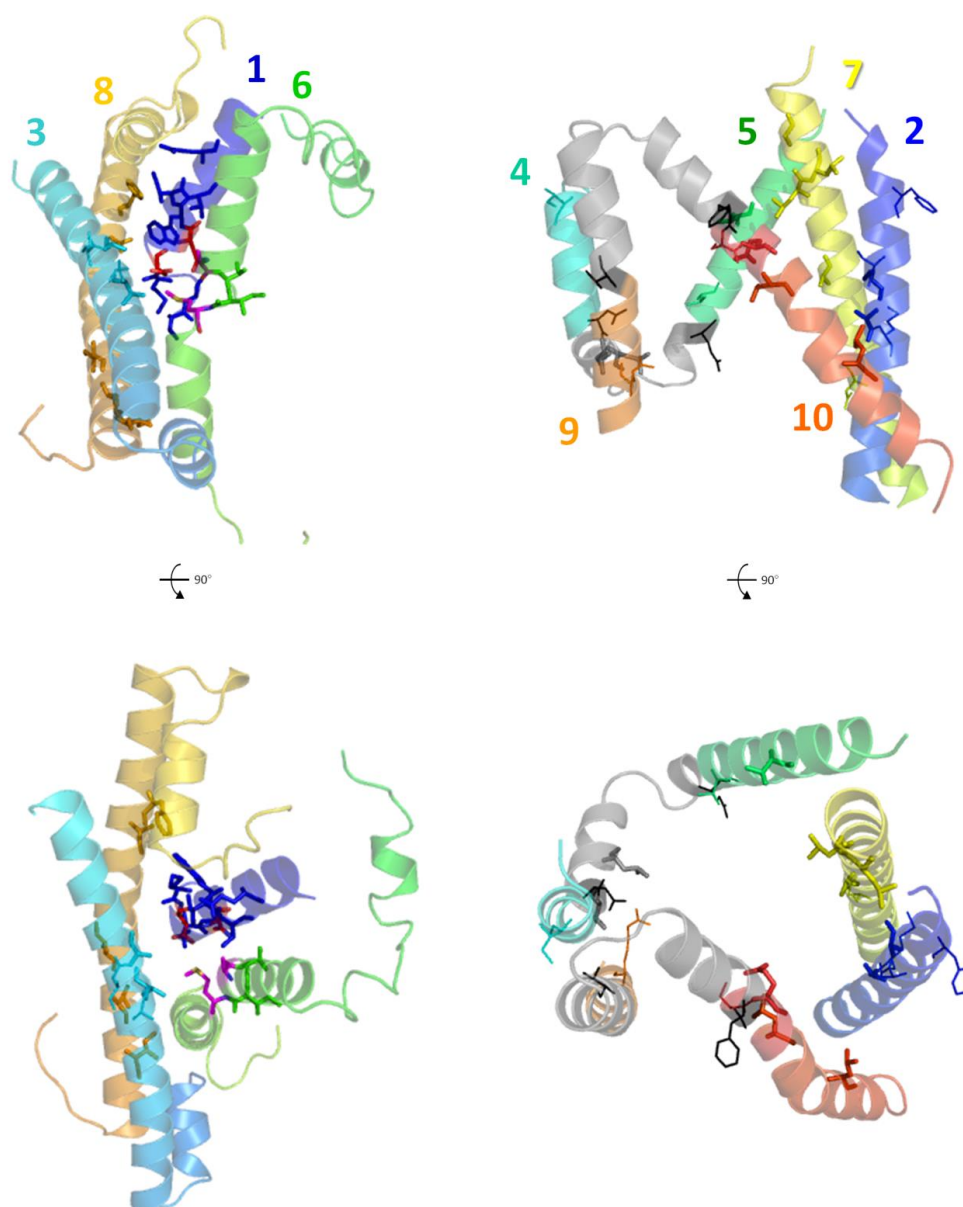


Figure 7. Candidate evolutionary rate-shifts distinguishing archetype from prototype Nramp (eukaryotic Slc11s). Left, protomer interface (TMS1, 3, 6 and 8), and right, carrier outer fence (TMS2, 4, 5, 7, 9 and 10). Top panel, transversal view, bottom panel, view from the membrane exterior. Loops joining TMS4/5 and TMS9/10 that are part respectively, of the internal and external gates are indicated in grey; residues marking the boundaries are indicated by lines, whereas residues corresponding to putative archetype vs prototype Nramp evolutionary rate-shifts are represented by sticks.

ScaDMT residues corresponding to sites that diverged between Nramp types, and which may interact with each other (within 5 Å distance in the inwardly-open structure), locate primarily at the protomer interface in the central area of the membrane plane (Figure 7). These sites are frequently adjacent to Slc11-specific sites and/or residues inferred to exert functional roles based on structural homology with known APC structures (Tables 1 and 3). About 19 Nramp type-specific sites form

three potential networks that involve TMS1, 3, 6, 10; TMS2, 6, 10 or TMS1, 2, 5, 7 and 8 (Table 3). These possible interactions may influence discrete steps in carrier cycling, such as substrate binding and extracellular gating, substrate binding and bundle rocking or co-substrate binding and intracellular gating, respectively.

As 3D mapping suggests, Nramp type-specific sites may modulate carrier activity. Since a majority of sites (27/38) demonstrate divergence of archetype Nramp, compared to the rest of Slc11 family, it is suggested the corresponding amino acid residues may play functional roles that differentiate archetype from prototype Nramp activity. Assuming that archetype Nramp antimicrobial role emerged early in eukaryotic evolution (i.e., before divergence of animals, amoebae and plants), it is plausible that pathogen-driven selective pressure stimulated archetype Nramp functional adaptation which resulted in significant sequence divergence from prototype Nramp (Table 2).

This proposition seems corroborated by past mutagenesis experiments where reciprocal amino acid exchanges between yeast Smf1p (SceASCpNR1) and rat DCT1 (ortholog of HsaMETaNR2) affected both metal and proton uptake [88]. Table 3 shows that in fact, the targeted sites distinguish archetype from prototype Nramp (i.e., I⁵⁴, Q⁵⁸; [89]) whereas functional studies showed greater impact on the residue that is more conserved (Q⁵⁸; [88]). Reciprocal exchange of Nramp-type rate-shifted sites thus holds potential to provide functional information on Slc11 metal and proton uptake activity.

3.8. Divergence in metal-uncoupled regulatory leaks of monovalent cation (Na⁺ or H⁺)

Mechanistic difference also has surfaced upon comparison of yeast Smf1p and rat DCT1 electro-physiological properties. Both prototype and archetype Nramp activities were associated with metal induced uncoupled currents (leaks), indicating increased uptake of monovalent cations which were thought to limit excessive metal influx that would otherwise be cytotoxic. But the nature of these uncoupled currents differ. Smf1p activity was associated with Na⁺ leak, notably at alkaline pH [90], and sodium-dependent inhibition of metal uptake was confirmed using another fungal prototype Nramp (both from *Dikarya* spp.; [91]). In contrast, currents uncoupled from metal uptake that were observed with archetype Nramp2/Dmt1 constitute a H⁺ leak, notably observed at acidic pH or in conditions of negative membrane potential [90,92,93].

Nramp metal substrates are potentially cytotoxic: excessive iron may lead to formation of oxygen radicals that damage cellular structures and macromolecules; inactivation of iron-based enzymes may result from over-accumulation of Mn and subsequent displacement of Fe co-factors; and Co and Cd are highly cytotoxic heavy metals [94,95]. Slc11-dependent metal uncoupled currents may thus represent an intrinsic protective mechanism that prevents metal over-accumulation [90,93]. The difference between Smf1p and rat DCT1 leak currents contrasts with otherwise similar properties, such as metal-ion selectivity and proton-coupled metal uptake, and its significance is currently unknown. It could be instructive to examine whether Na⁺ vs H⁺ leaks reflect functional divergence between prototype and archetype Nramp.

Na⁺ is the predominant motive force used in the APC superfamily. However, some APC carriers use protons instead of sodium ions to drive transport: the H⁺-driven amino acid importer ApcT (Slc7 family) apparently evolved from Na⁺-dependent transport, as ApcT K¹⁵⁸ mediates proton coupled transport with the amine group fulfilling a role analogous to Na² ion in LeuT [21]. Another carrier part of the APC superfamily, the arginine-agmatine antiporter (AdiC, Slc12), demonstrated also

proton-dependent activity [22,96]. These studies indicate prevalence of proton-coupled mechanisms among APC carriers, and possible adaptation from one type of energy coupling mechanism (using Na^+) to another (based on H^+).

Accordingly, fungal prototype Nramp interaction with Na^+ may reflect Slc11 evolutionary origins, which link these carriers to the APC superfamily and predominant utilization of Na^+ electrochemical gradient. Alternatively, Na^+ leak currents observed with dikaryal prototype Nramps [90,91] may result from specific divergence in the common ancestor of ascomycetes and basidiomycetes, since all currently known genomes from both taxa (541 genomes, DOE JGI Mycocosm) lack archetype Nramp but display instead highly divergent prototype Nramps (e.g., ScaASCpNR1, compared to DdiAMB_pNR; Table 2). Additional studies of prototype Nramp from different taxa will likely help characterizing regulatory leak currents, while reviewing existing data in light of site-specific rate variations may also provide clues.

3.9. Functional divergence between prototype and archetype Nramp?

Transport studies indicated that the functional properties of Slc11 carriers have been highly conserved between prokaryotic and eukaryotic homologs. Hence, carriers from both bacteria (MntH) and eukaryotes (Nramp) use the electrochemical gradient of the proton to drive metal uptake [42,92,97,98]. This suggests this mechanism of active transport may date back to Slc11 origin [12,43]. In addition, all Slc11 carriers demonstrate high affinity for Cd^{2+} [2,43]. However, bacterial MntH clearly prefer Mn over Fe [99–102] while eukaryotic Slc11 display similar affinities for both metals [2,93]. Available data thus suggest that despite variations in metal selectivity MntH and Nramp homologs share a common necessity that is to regulate and limit Cd^{2+} accumulation.

Proton import mediated by *Escherichia coli* MntH is induced more strongly by Cd^{2+} compared to Mn^{2+} (and also Fe^{2+} and Co^{2+}), and Cd^{2+} -induced proton uptake was further augmented by mutation of TMS11 Slc11-specific N^{411} [32]. Accordingly, metal-induced H^+ leak may be a common property of both MntH and Nramp and consequently, Na^+ leak reported for fungal (or dikaryal) prototype Nramp may indicate specific adaptation. The existence of fungal spp. carrying both prototype and archetype Nramp and the presence of prototype Nramp in various phyla (e.g., Table 2) allow testing this hypothesis, by comparing metal-uncoupled regulatory leak activities between prototype Nramp from various spp. and/or between prototype and archetype from a single species.

Sequence divergence between prototype and archetype Nramp previously revealed mechanistic connections to metal uncoupled currents, after experimental exchange of corresponding residues [88]. As murine mutations had revealed the functional importance of Slc11 TMS4, with loss of function mutations G169D in Nramp1 [6] and G185R in Nramp2/Dmt1 [103], this TMS was targeted for mutagenesis of a site that differs between prototype and archetype Nramps ([104]; cf ScaDMT L^{157} , Table 3, which corresponds to Dmt1 F^{196}).

Dmt1 F^{196} is located on the same face of TMS4 as G^{185} ; in ScaDMT structure this helix face is directed towards the inner core of the transporter, and L^{157} locates in the portion of the helix that bends upon opening of the inner gate [8]. Remarkably, exchange of Dmt1 F^{196} for the corresponding Smf1p residue (Ile) drastically reduced Dmt1 H^+ leak while leaving uncompromised metal uptake selectivity and efficacy, as well as yeast *Smf1* mutant complementation ability [104]. Since the amino acid substitution F^{196}I is relatively conservative its functional impact implies the corresponding site contributes to Dmt1 activity. This interpretation seems consistent with a 3D location close to

ScaDMT pair of adjacent residues in TMS8, which appeared homologous to LeuT moieties part of the Na² binding site ([105]; Table 1) and might contribute to H⁺ binding by Slc11 carriers.

Dmt1 F196I exchange was reported to compensate for another mutation (I113F) in TMS2. This seems surprising as ScaDMT corresponding residue (Leu⁷⁶) has its side chain directed toward the membrane interior and was predicted to interact with modeled lipid tail [57]. ScaDMT Leu⁷⁶ corresponds to relatively minor variations among Nramp types: V, I, A (C, L)/(I, L, F (V)), which seem compatible with lipid-accessibility. Dmt1 mutation I113F was detrimental: it abolished metal uptake while increasing metal uncoupled currents, not only H⁺-dependent as expected for Dmt1 but also Na⁺-dependent [106]. Neither reducing external proton concentration nor substitution of Na⁺ for choline restored metal uptake, indicating that I113F mutation not only inactivated Dmt1 metal-ion conduction pathway but also perturbed carrier interactions with monovalent cations. Yet Dmt1 double mutant I113F-F196I recovered divalent metal uptake ability and produced limited metal uncoupled currents [106].

Interpreting the above result from a structural point of view is not straightforward given the opposite locations of the mutated sites: neither site appears to be part of the transporter ion conduction pathway so that the reported phenotype must be the result of some indirect effect. Slc11 TMS2 was predicted to undergo significant motion during carrier cycling (Figure 6); Dmt1 mutation I113F may perturb TMS2 interactions with lipids, and maybe with neighbor helix (TMS6), so that metal-ion transport is impeded as well as the selectivity of carrier interaction with monovalent cations.

Similarly, Dmt1 mutation F196I may disturb TMS4 interaction with TMS8 and impact on Dmt1 capacity to transport monovalent cations. Part of the explanation for the observed phenotypes may also reside in the fact that both sites represent potential evolutionary rate-shifts and may be part of a network of coevolved sites that tune Dmt1 activity. Experimental testing of the role of archetype-specific sites in cation transport activities will likely yield better understanding of eukaryotic Slc11 carrier mechanism.

4. Conclusion

Studying Slc11 molecular evolution in the context of 3D structure adds some functional dimension to the knowledge of how the transporter structure emerged and evolved [107]. Previous efforts at the interface of structural biology and molecular evolution allowed to distinguish the Slc11 family of proton-dependent transporters of transition metal-ions from a phylogenetic outgroup of Mg²⁺ carriers [32,41,42,54,62]. Analyses presented herein argue that further investigation of Slc11 carrier evolution in light of 3D structure will inform molecular understanding of transport activity of Slc11 carriers and their roles in physiology and immunity.

Resolution of ScaDMT structure provided a key asset to decipher Slc11 carrier function at the molecular level [8]; it fostered realization that the Slc11 family belongs to the APC superfamily, which is defined by the LeuT-fold and characterized by notably diverse substrates and transport-driving cations. The APC superfamily also displays broad phylogenetic distribution as the second largest superfamily of secondary carriers after the Major facilitator superfamily (MFS; [9]). Accordingly Slc11 carriers have ancient origins, which implies that remarkable sequence conservation in this family owes to important structural and/or functional constraints.

Three-dimensional mapping of Slc11-specific residues onto ScaDMT structure showed they

distribute mainly at the interface of LeuT-fold protomers, along the transmembrane ion-conduction pathway. Since the LeuT-fold protomer interface displays structural diversity within the APC superfamily, seemingly correlating with (co)substrates variety across APC families, the observed distribution of Slc11-specific residue implies they may contribute key interactions with the transported cosubstrates. In addition, a fraction of Slc11-specific sites (30%) exhibited potential contacts with surrounding molecules of lipids, as modeled by the MemProtMD pipeline, suggesting that protein-lipid contacts may influence Slc11 activity.

Homology threading using the ConTemplate pipeline required relaxed parameters to compensate for distant relationships between APC families. This approach generated hypothetical ScaDMT conformers based on known APC structures, showing that Slc11 architecture is compatible with discrete steps of LeuT-like carrier cycle (rocking bundle mechanism). Predicted ScaDMT conformers suggested Slc11 sites homologous to functional residues previously identified in APC templates. These sites overlapped with or were located nearby Slc11-specific residues, hence providing further support to the functional importance of Slc11-specific sites.

Sites that diverged between eukaryotic Slc11 (Nramp) types occupy TMS involved in discrete steps of cosubstrate translocation. Half of the corresponding residues may interact with each other, potentially creating networks involving TMS1-3, 5-8 and 10. Besides, a fraction of Nramp type-specific sites (30%) was predicted with MemProtMD pipeline to interact with surrounding lipids. These findings suggest that Nramp type-specific sites may modulate Nramp activity through different types of interactions involving amino acid residues and/or lipids.

Together these analyses demonstrate both the informativeness of a phylogenetic approach that targets evolutionary rate-shifted sites in a 3D context and its usefulness in mutagenesis studies that explore structure/function relationships and carrier mechanism. In particular, reciprocal exchange of group-specific residues has potential to instruct in understanding Slc11 metal and proton uptake activity, and seeking mutations that may stabilize some conformer constitutes an important aim for future studies.

Acknowledgments

The NCBI, DOE-JGI and Broad sequencing communities and online facilities are gratefully acknowledged, as well as Dr Ben-Tal and Narunsky for their help using the ConTemplate server. The author received no specific funding for this work.

Conflict of Interest

All authors declare no conflict of interest in this paper.

References

1. Hediger MA, Clemencon B, Burrier RE, et al. (2013) The ABCs of membrane transporters in health and disease (SLC series): introduction. *Mol Aspects Med* 34: 95–107.
2. Illing AC, Shawki A, Cunningham CL, et al. (2012) Substrate profile and metal-ion selectivity of human divalent metal-ion transporter-1. *J Biol Chem* 287: 30485–30496.
3. Cellier MF (2013) Cell-Type Specific Determinants of NRAMP1 Expression in Professional

- Phagocytes. *Biology (Basel)* 2: 233–283.
4. Braasch I, Gehrke AR, Smith JJ, et al. (2016) The spotted gar genome illuminates vertebrate evolution and facilitates human-teleost comparisons. *Nat Genet* 48: 427–437.
 5. Cellier MF, Courville P, Champion C (2007) Nramp1 phagocyte intracellular metal withdrawal defense. *Microbes Infect* 9: 1662–1670.
 6. Vidal SM, Malo D, Vogan K, et al. (1993) Natural resistance to infection with intracellular parasites: isolation of a candidate for Bcg. *Cell* 73: 469–485.
 7. Peracino B, Wagner C, Balest A, et al. (2006) Function and mechanism of action of Dictyostelium Nramp1 (Slc11a1) in bacterial infection. *Traffic* 7: 22–38.
 8. Ehrnstorfer IA, Geertsma ER, Pardon E, et al. (2014) Crystal structure of a SLC11 (NRAMP) transporter reveals the basis for transition-metal ion transport. *Nat Struct Mol Biol* 21: 990–996.
 9. Vastermark A, Wollwage S, Houle ME, et al. (2014) Expansion of the APC superfamily of secondary carriers. *Proteins* 82: 2797–2811.
 10. Yamashita A, Singh SK, Kawate T, et al. (2005) Crystal structure of a bacterial homologue of Na⁺/Cl⁻-dependent neurotransmitter transporters. *Nature* 437: 215–223.
 11. Forrest LR (2015) Structural Symmetry in Membrane Proteins. *Annu Rev Biophys* 44: 311–337.
 12. Cellier MF (2012) Nutritional immunity: homology modeling of Nramp metal import. *Adv Exp Med Biol* 946: 335–351.
 13. Shi Y (2013) Common Folds and Transport Mechanisms of Secondary Active Transporters. *Annu Rev Biophys* 42: 51–72.
 14. Kowalczyk L, Ratera M, Paladino A, et al. (2011) Molecular basis of substrate-induced permeation by an amino acid antiporter. *Proc Natl Acad Sci USA* 108: 3935–3940.
 15. Krishnamurthy H, Piscitelli CL, Gouaux E (2009) Unlocking the molecular secrets of sodium-coupled transporters. *Nature* 459: 347–355.
 16. Forrest LR, Kramer R, Ziegler C (2011) The structural basis of secondary active transport mechanisms. *Biochim Biophys Acta* 1807: 167–188.
 17. Faham S, Watanabe A, Besserer GM, et al. (2008) The crystal structure of a sodium galactose transporter reveals mechanistic insights into Na⁺/sugar symport. *Science* 321: 810–814.
 18. Weyand S, Shimamura T, Yajima S, et al. (2008) Structure and molecular mechanism of a nucleobase-cation-symport-1 family transporter. *Science* 322: 709–713.
 19. Ressler S, Terwisscha van Scheltinga AC, Vonrhein C, et al. (2009) Molecular basis of transport and regulation in the Na⁽⁺⁾/betaine symporter BetP. *Nature* 458: 47–52.
 20. Gao X, Lu F, Zhou L, et al. (2009) Structure and mechanism of an amino acid antiporter. *Science* 324: 1565–1568.
 21. Shaffer PL, Goehring A, Shankaranarayanan A, et al. (2009) Structure and mechanism of a na⁺-independent amino Acid transporter. *Science* 325: 1010–1014.
 22. Fang Y, Jayaram H, Shane T, et al. (2009) Structure of a prokaryotic virtual proton pump at 3.2 Å resolution. *Nature* 460: 1040–1043.
 23. Gao X, Zhou L, Jiao X, et al. (2010) Mechanism of substrate recognition and transport by an amino acid antiporter. *Nature* 463: 828–832.
 24. Tang L, Bai L, Wang WH, et al. (2010) Crystal structure of the carnitine transporter and insights into the antiport mechanism. *Nat Struct Mol Biol* 17: 492–496.
 25. Shimamura T, Weyand S, Beckstein O, et al. (2010) Molecular basis of alternating access membrane transport by the sodium-hydantoin transporter Mhp1. *Science* 328: 470–473.

26. Schulze S, Koster S, Geldmacher U, et al. (2010) Structural basis of Na(+)-independent and cooperative substrate/product antiport in CaiT. *Nature* 467: 233–236.
27. Krishnamurthy H, Gouaux E (2012) X-ray structures of LeuT in substrate-free outward-open and apo inward-open states. *Nature* 481: 469–474.
28. Ma D, Lu P, Yan C, et al. (2012) Structure and mechanism of a glutamate-GABA antiporter. *Nature* 483: 632–636.
29. Khafizov K, Perez C, Koshy C, et al. (2012) Investigation of the sodium-binding sites in the sodium-coupled betaine transporter BetP. *Proc Natl Acad Sci USA* 109: E3035–E3044.
30. Perez C, Faust B, Mehdipour AR, et al. (2014) Substrate-bound outward-open state of the betaine transporter BetP provides insights into Na⁺ coupling. *Nat Commun* 5: 4231.
31. Malinauskaite L, Quick M, Reinhard L, et al. (2014) A mechanism for intracellular release of Na⁺ by neurotransmitter/sodium symporters. *Nat Struct Mol Biol* 21: 1006–1012.
32. Chaloupka R, Courville P, Veyrier F, et al. (2005) Identification of functional amino acids in the Nramp family by a combination of evolutionary analysis and biophysical studies of metal and proton cotransport in vivo. *Biochemistry* 44: 726–733.
33. Gaucher EA, Gu X, Miyamoto MM, et al. (2002) Predicting functional divergence in protein evolution by site-specific rate shifts. *Trends Biochem Sci* 27: 315–321.
34. Knudsen B, Miyamoto MM, Laipis PJ, et al. (2003) Using Evolutionary Rates to Investigate Protein Functional Divergence and Conservation. A case study of the carbonic anhydrases. *Genetics* 164: 1261–1269.
35. Gu X, Vander Velden K (2002) DIVERGE: phylogeny-based analysis for functional-structural divergence of a protein family. *Bioinformatics* 18: 500–501.
36. Gu X, Zou Y, Su Z, et al. (2013) An update of DIVERGE software for functional divergence analysis of protein family. *Mol Biol Evol* 30: 1713–1719.
37. Echave J, Spielman SJ, Wilke CO (2016) Causes of evolutionary rate variation among protein sites. *Nat Rev Genet* 17: 109–121.
38. Zhang J, Yang JR (2015) Determinants of the rate of protein sequence evolution. *Nat Rev Genet* 16: 409–420.
39. Sandler I, Zigdon N, Levy E, et al. (2014) The functional importance of co-evolving residues in proteins. *Cell Mol Life Sci* 71: 673–682.
40. de Juan D, Pazos F, Valencia A (2013) Emerging methods in protein co-evolution. *Nat Rev Genet* 14: 249–261.
41. Shin JH, Wakeman CA, Goodson JR, et al. (2014) Transport of magnesium by a bacterial nramp-related gene. *PLoS Genet* 10: e1004429.
42. Courville P, Urbankova E, Rensing C, et al. (2008) Solute carrier 11 cations symport requires distinct residues in transmembrane helices 1 and 6. *J Biol Chem* 283: 9651–9658.
43. Cellier MF (2012) Nramp: from sequence to structure and mechanism of divalent metal import. *Curr Top Membr* 69: 249–293.
44. Richer E, Courville P, Cellier M (2004) Molecular Evolutionary Analysis of the Nramp Family. Cellier M. and Gros P. (eds) *Molecular biology intelligence unit*. 178–194. Springer.
45. Richer E, Courville P, Bergevin I, et al. (2003) Horizontal gene transfer of "prototype" Nramp in bacteria. *J Mol Evol* 57: 363–376.
46. Jenuth JP (2000) The NCBI. Publicly available tools and resources on the Web. *Methods Mol Biol* 132: 301–312.

47. Biegert A, Mayer C, Remmert M, et al. (2006) The MPI Bioinformatics Toolkit for protein sequence analysis. *Nucleic Acids Res* 34: W335–W339.
48. Tamura K, Peterson D, Peterson N, et al. (2011) MEGA5: molecular evolutionary genetics analysis using maximum likelihood, evolutionary distance, and maximum parsimony methods. *Mol Biol Evol* 28: 2731–2739.
49. Thompson JD, Gibson TJ, Higgins DG (2002) Multiple sequence alignment using ClustalW and ClustalX. *Curr Protoc Bioinform* Chapter 2: Unit 2.3.: Unit.
50. Gouy M, Guindon S, Gascuel O (2010) SeaView Version 4: A Multiplatform Graphical User Interface for Sequence Alignment and Phylogenetic Tree Building. *Mol Biol Evol* 27: 221–224.
51. Burki F (2014) The Eukaryotic Tree of Life from a Global Phylogenomic Perspective. *Cold Spring Harbor Perspectives in Biology* 6. a016147.
52. Koonin EV (2010) The origin and early evolution of eukaryotes in the light of phylogenomics. *Genome Biol* 11: 209.
53. Adl SM, Simpson AGB, Lane CE, et al. (2012) The Revised Classification of Eukaryotes. *J Eukaryot Microbiol* 59: 429–493.
54. Lin Z, Fernandez-Robledo JA, Cellier MF, et al. (2011) The natural resistance-associated macrophage protein from the protozoan parasite *Perkinsus marinus* mediates iron uptake. *Biochemistry* 50: 6340–6355.
55. Guindon S, Dufayard JF, Lefort V, et al. (2010) New algorithms and methods to estimate maximum-likelihood phylogenies: assessing the performance of PhyML 3.0. *Syst Biol* 59: 307–321.
56. Shih AC, Lee DT, Peng CL, et al. (2007) Phylo-mLogo: an interactive and hierarchical multiple-logo visualization tool for alignment of many sequences. *BMC Bioinformatics* 8: 63.
57. Stansfeld PJ, Goose JE, Caffrey M, et al. (2015) MemProtMD: Automated Insertion of Membrane Protein Structures into Explicit Lipid Membranes. *Structure* 23: 1350–1361.
58. DeLano WL (2002) The PyMOL Molecular Graphics System. DeLano Scientific, San carlos, california, USA. Available from: <http://www.pymol.org>.
59. Ye Y, Godzik A (2003) Flexible structure alignment by chaining aligned fragment pairs allowing twists. *Bioinformatics* 19 Suppl 2: ii246–ii255.
60. Pieper U, Webb BM, Barkan DT, et al. (2011) ModBase, a database of annotated comparative protein structure models, and associated resources. *Nucleic Acids Res* 39: D465–D474.
61. Narunsky A, Nepomnyachiy S, Ashkenazy H, et al. (2015) ConTemplate Suggests Possible Alternative Conformations for a Query Protein of Known Structure. *Structure* 23: 2162–2170.
62. Czachorowski M, Lam-Yuk-Tseung S, Cellier M, et al. (2009) Transmembrane Topology of the Mammalian Slc11a2 Iron Transporter. *Biochemistry* 48: 8422–8434.
63. Xia J, Yamaji N, Kasai T, et al. (2010) Plasma membrane-localized transporter for aluminum in rice. *Proc Natl Acad Sci USA* 107: 18381–18385.
64. Pottier M, Oomen R, Picco C, et al. (2015) Identification of mutations allowing Natural Resistance Associated Macrophage Proteins (NRAMP) to discriminate against cadmium. *Plant J* 83: 625–637.
65. Tavoulari S, Margheritis E, Nagarajan A, et al. (2016) Two Na⁺ Sites Control Conformational Change in a Neurotransmitter Transporter Homolog. *J Biol Chem* 291: 1456–1471.
66. Ashkenazy H, Erez E, Martz E, et al. (2010) ConSurf 2010: calculating evolutionary conservation in sequence and structure of proteins and nucleic acids. *Nucleic Acids Res* 38:

W529–W533.

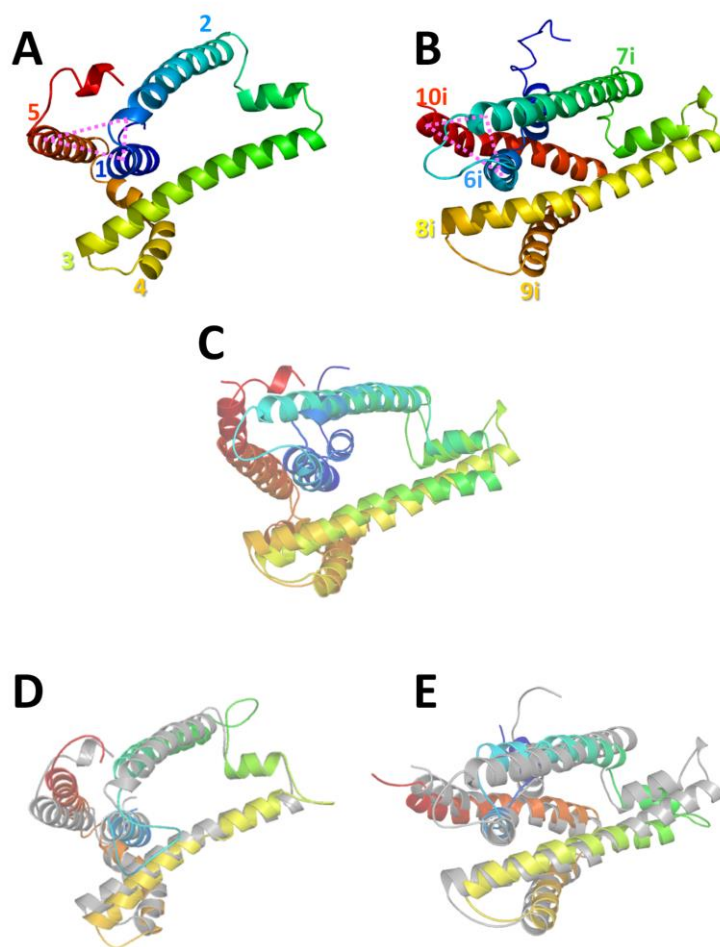
67. De Falco L, Bruno M, Andolfo I, et al. (2012) Identification and characterization of the first SLC11A2 isoform 1a mutation causing a defect in splicing process and an hypomorphic allele expression of the SLC11A2 gene. *Br J Haematol* 159: 492–495.
68. Bardou-Jacquet E, Island ML, Jouanolle AM, et al. (2011) A novel N491S mutation in the human SLC11A2 gene impairs protein trafficking and in association with the G212V mutation leads to microcytic anemia and liver iron overload. *Blood Cells Mol Dis* 47: 243–248.
69. Blanco E, Kannengiesser C, Grandchamp B, et al. (2009) Not all DMT1 mutations lead to iron overload. *Blood Cells Mol Dis* 43: 199–201.
70. Iolascon A, De FL (2009) Mutations in the gene encoding DMT1: clinical presentation and treatment. *Semin Hematol* 46: 358–370.
71. Iolascon A, d'Apolito M, Servedio V, et al. (2006) Microcytic anemia and hepatic iron overload in a child with compound heterozygous mutations in DMT1 (SCL11A2) *Blood* 107: 349–354.
72. Iolascon A, Camaschella C, Pospisilova D, et al. (2008) Natural history of recessive inheritance of DMT1 mutations. *J Pediatr* 152: 136–139.
73. Mims MP, Guan Y, Pospisilova D, et al. (2005) Identification of a human mutation of DMT1 in a patient with microcytic anemia and iron overload. *Blood* 105: 1337–1342.
74. Simmons KJ, Jackson SM, Brueckner F, et al. (2014) Molecular mechanism of ligand recognition by membrane transport protein, Mhp1. *EMBO J* 33: 1831–1844.
75. Alva V, Soding J, Lupas AN (2015) A vocabulary of ancient peptides at the origin of folded proteins. *Elife* 4.
76. Das S, Dawson NL, Orengo CA (2015) Diversity in protein domain superfamilies. *Curr Opin Genet Dev* 35: 40–49.
77. Vergara-Jaque A, Fenollar-Ferrer C, Kaufmann D, et al. (2015) Repeat-swap homology modeling of secondary active transporters: updated protocol and prediction of elevator-type mechanisms. *Front Pharmacol* 6: 183.
78. Siddle KJ, Quintana-Murci L (2014) The Red Queen's long race: human adaptation to pathogen pressure. *Curr Opin Genet Dev* 29: 31–38.
79. Nakashige TG, Zhang B, Krebs C, et al. (2015) Human calprotectin is an iron-sequestering host-defense protein. *Nat Chem Biol* 11: 765–771.
80. Becker KW, Skaar EP (2014) Metal limitation and toxicity at the interface between host and pathogen. *FEMS Microbiol Rev* 38: 1235–1249.
81. Lisher JP, Giedroc DP (2013) Manganese acquisition and homeostasis at the host-pathogen interface. *Front Cell Infect Microbiol* 3: 91.
82. Ganz T (2009) Iron in innate immunity: starve the invaders. *Curr Opin Immunol* 21: 63–67.
83. Ganz T, Nemeth E (2015) Iron homeostasis in host defence and inflammation. *Nat Rev Immunol* 15: 500–510.
84. Buracco S, Peracino B, Cinquetti R, et al. (2015) Dictyostelium Nramp1, which is structurally and functionally similar to mammalian DMT1 transporter, mediates phagosomal iron efflux. *J Cell Sci* 128: 3304–3316.
85. Gallant CJ, Malik S, Jabado N, et al. (2007) Reduced in vitro functional activity of human NRAMP1 (SLC11A1) allele that predisposes to increased risk of pediatric tuberculosis disease. *Genes Immun* 8: 691–698.
86. Desiro A, Salvioli A, Ngonkeu EL, et al. (2014) Detection of a novel intracellular microbiome

- hosted in arbuscular mycorrhizal fungi. *ISME J* 8: 257–270.
87. Ohshima S, Sato Y, Fujimura R, et al. (2016) Mycoavidus cysteinexigens gen. nov., sp. nov., an endohyphal bacterium isolated from a soil isolate of the fungus Mortierella elongata. *Int J Syst Evol Microbiol*.
 88. Cohen A, Nevo Y, Nelson N (2003) The first external loop of the metal ion transporter DCT1 is involved in metal ion binding and specificity. *Proc Natl Acad Sci USA* 100: 10694–10699.
 89. Courville P, Chaloupka R, Cellier MF (2006) Recent progress in structure-function analyses of Nramp proton-dependent metal-ion transporters. *Biochem Cell Biol* 84: 960–978.
 90. Chen X, Peng J, Cohen A, et al. (1999) Yeast SMF1 mediates H⁺-coupled iron uptake with concomitant uncoupled cation currents. *J Biol Chem* 274: 35089–35094.
 91. Agranoff D, Collins L, Kehres D, et al. (2005) The Nramp orthologue of Cryptococcus neoformans is a pH-dependent transporter of manganese, iron, cobalt and nickel. *Biochem J* 385: 225–232.
 92. Gunshin H, Mackenzie B, Berger UV, et al. (1997) Cloning and characterization of a mammalian proton-coupled metal-ion transporter. *Nature* 388: 482–488.
 93. Sacher A, Cohen A, Nelson N (2001) Properties of the mammalian and yeast metal-ion transporters DCT1 and Smf1p expressed in Xenopus laevis oocytes. *J Exp Biol* 204: 1053–1061.
 94. Bleackley MR, MacGillivray RT (2011) Transition metal homeostasis: from yeast to human disease. *Biometals* 24: 785–809.
 95. Martin JE, Waters LS, Storz G, et al. (2015) The Escherichia coli small protein MntS and exporter MntP optimize the intracellular concentration of manganese. *PLoS Genet* 11: e1004977.
 96. Tsai MF, Fang Y, Miller C (2012) Sided functions of an arginine-arginine antiporter oriented in liposomes. *Biochemistry* 51: 1577–1585.
 97. Nevo Y, Nelson N (2006) The NRAMP family of metal-ion transporters. *Biochim Biophys Acta* 1763: 609–620.
 98. Lan WJ, Ren HL, Pang Y, et al. (2012) A facile transport assay for H⁺ coupled membrane transport using fluorescence probes. *Analytical Methods* 4: 44–46.
 99. Makui H, Roig E, Cole ST, et al. (2000) Identification of the Escherichia coli K-12 Nramp orthologue (MntH) as a selective divalent metal ion transporter. *Mol Microbiol* 35: 1065–1078.
 100. Kehres DG, Zaharik ML, Finlay BB, et al. (2000) The NRAMP proteins of Salmonella typhimurium and Escherichia coli are selective manganese transporters involved in the response to reactive oxygen. *Mol Microbiol* 36: 1085–1100.
 101. Perry RD, Mier I, Fetherston JD (2007) Roles of the Yfe and Feo transporters of Yersinia pestis in iron uptake and intracellular growth. *Biometals* 20: 699–703.
 102. Hohle TH, O'Brian MR (2009) The mntH gene encodes the major Mn(2+) transporter in Bradyrhizobium japonicum and is regulated by manganese via the Fur protein. *Mol Microbiol* 72: 399–409.
 103. Fleming MD, Trenor CC, Su MA, et al. (1997) Microcytic anaemia mice have a mutation in Nramp2, a candidate iron transporter gene. *Nat Genet* 16: 383–386.
 104. Nevo Y, Nelson N (2004) The mutation F227I increases the coupling of metal ion transport in DCT1. *J Biol Chem* 279: 53056–53061.
 105. Penmatsa A, Gouaux E (2014) How LeuT shapes our understanding of the mechanisms of

sodium-coupled neurotransmitter transporters. *J Physiol* 592: 863–869.

106. Nevo Y (2008) Site-directed mutagenesis investigation of coupling properties of metal ion transport by DCT1. *Biochim Biophys Acta* 1778: 334–341.
107. Ivankov DN, Finkelstein AV, Kondrashov FA (2014) A structural perspective of compensatory evolution. *Curr Opin Struct Biol* 26: 104–112.

Supplementary



Suppl. Figure 1. ScaDMT protomer asymmetry. **AB.** Comparative visualization of ScaDMT N-protomer (TMS1-5, A) and C-protomer represented with parallel topologies (i.e., the orientation of C-protomer has been inverted; TMS6i-10i, B). The protomers display alternate configurations, “closed” (N-protomer) and “open” (C-protomer), as indicated by dotted triangles joining TMS1, 2 and 5 (A) and TMS6i, 7i and 10i (B). **C.** Structural alignment of ScaDMT protomers using FATCAT flexible structure comparison [59] yielded 147 equivalent positions with an RMSD of 2.96 Å and with 2 twists. This structural alignment was used to align the respective protomer sequences and the sequence alignments were used to model alternate configurations for each protomer. **DE.**

Structural superimposition of ScaDMT native protomers (in grey) with models representing alternate configuration of the other protomer: N-protomer and C-protomer model (D), C-protomer and N-protomer model (E). The structural alignments showed 152 equivalent positions with an RMSD of 3.20 Å, without twists (D) and 165 equivalent positions with an RMSD of 2.88 Å, without twists (E).



AIMS Press

© 2016 Mathieu F. M. Cellier, licensee AIMS Press. This is an open access article distributed under the terms of the Creative Commons Attribution License (<http://creativecommons.org/licenses/by/4.0>)